Instabilities and Soot Formation in High-Pressure, Rich, Iso-Octane-Air Explosion Flames Part 1: Dynamical Structure

R.D. Lockett*, R. Woolley**

*School of Engineering and Mathematical Sciences, The City University,

Northampton Square, London EC1V 0HB, United Kingdom.

** Department of Mechanical Engineering, University of Sheffield,

Western Bank, Sheffield S10 2TN, United Kingdom.

Abstract

Simultaneous OH Planar Laser Induced Fluorescence (PLIF) and Rayleigh scattering measurements have been performed on 2 bar, rich, iso-octane-air explosion flames obtained in the optically accessible Leeds combustion bomb. Separate shadowgraph high-speed video images have been obtained from explosion flames at similar mixture conditions. Shadowgraph images, quantitative Rayleigh images and normalised OH concentration images have been presented for a selection of these explosion flames. Normalised experimental equilibrium OH concentrations behind the flame fronts have been compared with normalised, computed equilibrium OH concentrations as a function of equivalence ratio. The ratio of super-equilibrium OH concentration in the flame front to equilibrium OH concentration behind the flame front reveals the response of the flame to the thermal-diffusive instability, and the resistance of the flame front to rich quenching. Burned gas temperatures have been determined from the Rayleigh scattering images in the range $1.4 \leq \phi \leq 1.9$, and are found to be in good agreement with the corresponding predicted adiabatic flame temperatures. Soot formation was observed to occur behind deep cusps associated with large wavelength cracks occurring in the flame front for equivalence ratio $\phi \geq 1.8$ (C/O ≥ 0.576). The reaction time-scale for iso-octane pyrolysis to soot formation has been estimated to be approximately 7.5 ms – 10 ms.

Corresponding author: r.d.lockett@city.ac.uk
Tel: 44 (0) 207 040 8812 Fax: 44 (0) 207 040 8566

NOMENCLATURE

r	Flame radius (mm)
d	Flame diameter (mm)
D_{oxygen}	Molecular diffusivity of deficient reactant (m^2/s)
f	Lens f number
F	Focal length (cm)
I	Laser spectral flux density (W/(m^2.GHz))
I_{Sat}	Laser saturation spectral flux density (W/(m^2.GHz))
Le	Lewis number
Le*	Critical Lewis number
α	Thermal diffusivity (m^2/s)
t	Time (ms)
ϕ	Equivalence ratio
P	Pressure (bar)
T	Temperature (K)

1. INTRODUCTION

High pressure laminar explosion flames are susceptible to the development of surface cracks, which evolve into a cellular surface structure [1 – 8]. Linear stability analysis shows that, if a deformation occurs in the surface of a spherically expanding, laminar explosion flame during its early development, hydrodynamic and thermal-diffusive instabilities will be stabilised by the flame stretch until a critical Peclet number is reached [1 – 3]. After this critical radius, the flame becomes unstable to surface perturbations, which grow on the flame surface through the development of propagating cracks and cellular fission [1, 4].

Cellularity in flames with positive Markstein numbers is caused by the Darrieus-Landau hydrodynamic instability [5, 8]. This is of current interest as the determination of the experimental stretch-free laminar burning velocity becomes problematic as the flames become cellular. It might be suggested that use of a stretch-free laminar burning velocity is inappropriate at high pressures as it does not physically exist [9].

At low Lewis numbers (Le = α/D_{oxygen} < Le* $\approx$ 1), a smaller length-scale cellularity is observed to develop over the flame surface. This is in addition to the cellular structure formed as a result of the influence of the hydrodynamic instability [1, 8]. The smaller length-scale surface cellularity develops through the influence of the thermal-diffusive instability. The OH concentration and the rate of fuel oxidation in the concave regions of the flame surface (cusps/troughs) are reduced through the locally large negative flame stretch, while the OH concentration and rate of fuel oxidation in convex regions of the flame surface is raised through positive flame stretch [1]. It appears that the hydrodynamic instability has a short wavelength cut-off, which is significantly larger than the length scale over which the thermal-diffusive instability affects the flame surface [8]. At high pressures, this can result in a decoupling of the length-scales over which the hydrodynamic and thermal diffusive instability affect the flame surface [8, 10, 13].

Rich, high pressure, iso-octane-air laminar explosion flames susceptible to instability are presently unable to be investigated through detailed modelling. The iso-octane-air combustion mechanism is very complex, involving many hundreds of species in thousands of reactions. Much of the rich iso-octane-air combustion mechanism is

unknown. This leaves the theoretical development of simple combustion models, together with the application of suitable diagnostics as the basis for investigation of these types of flames. In recent years, numerical simulation of cellular flames has been able to demonstrate the underlying physics of cellular flames [11 – 13]. However, the chemistry models employed are usually relatively limited, one-step mechanisms being typical [7, 13].

Combustion strategies often adopt fuel staging or result in partial premixing, where the flame burns through locally rich mixtures. This can lead to soot formation in the burned mixture behind the flame front, where there is interaction between the cellular flame structure and the flame chemistry.

Soot formation has been the subject of extensive theoretical, modelling and experimental investigation over the last thirty years. A number of recent reviews have presented different perspectives on the subject [14 – 19]. Most laboratory studies of soot formation have employed non-intrusive optical diagnostics and/or probe techniques to investigate soot loading, size distribution, particle growth, morphology, and oxidation, using either premixed, partially premixed, or non-premixed flames, usually in a one-dimensional configuration.

Soot formed during explosions of rich iso-octane-air mixtures at high pressure was investigated using laser induced incandescence (LII) and Mie scattering in an optically accessible combustion bomb by Tait [20]. He found that soot was formed in a honeycomb-like structure behind the flame front, and drew the conclusion that these honeycomb-like structures were linked to the instability induced cellular structure of the flame. This phenomenon has also been identified during the combustion of rich mixtures formed in a direct injection s.i. engine using a swirl pressure atomiser [21]. Lockett *et al* have investigated this conclusion further, resulting in the identification of soot being formed behind deep cracks in the flame front, usually linked with the larger length-scale cracks induced by the hydrodynamic instability [8, 10].

The present work is the first of two papers exploring the relationship between cellular flame structure and soot formation in laminar, high pressure, rich, iso-octane-air explosion flames. This paper (Part 1) reports the results of an experimental study of

cellular explosion flames near the critical equivalence ratio for soot formation. The experiments were performed in a spherical explosion bomb with excellent optical access for the application of optical and laser diagnostics. Simultaneous OH planar laser induced fluorescence and planar Rayleigh scattering were employed to provide information about the local flame structure, soot formation and the local temperature field. Separate shadowgraph high-speed video images were obtained from explosion flames at similar conditions, in order to provide information on the flame expansion, and the dynamical behaviour of the flame surface.

The overall objectives of the present work (Part 1) were the experimental identification of the following combustion phenomena in high pressure, iso-octane-air, laminar explosion flames:

1. The determination of the dynamical behaviour and general structure of high pressure, low Lewis number iso-octane-air laminar explosion flames.
2. The determination of the critical equivalence ratio for soot formation.
3. The determination of the relationship between soot formation and the structure of the flame in the neighbourhood of the critical equivalence ratio.
4. The response of the flame to mixture enrichment in the neighbourhood of the critical equivalence ratio.
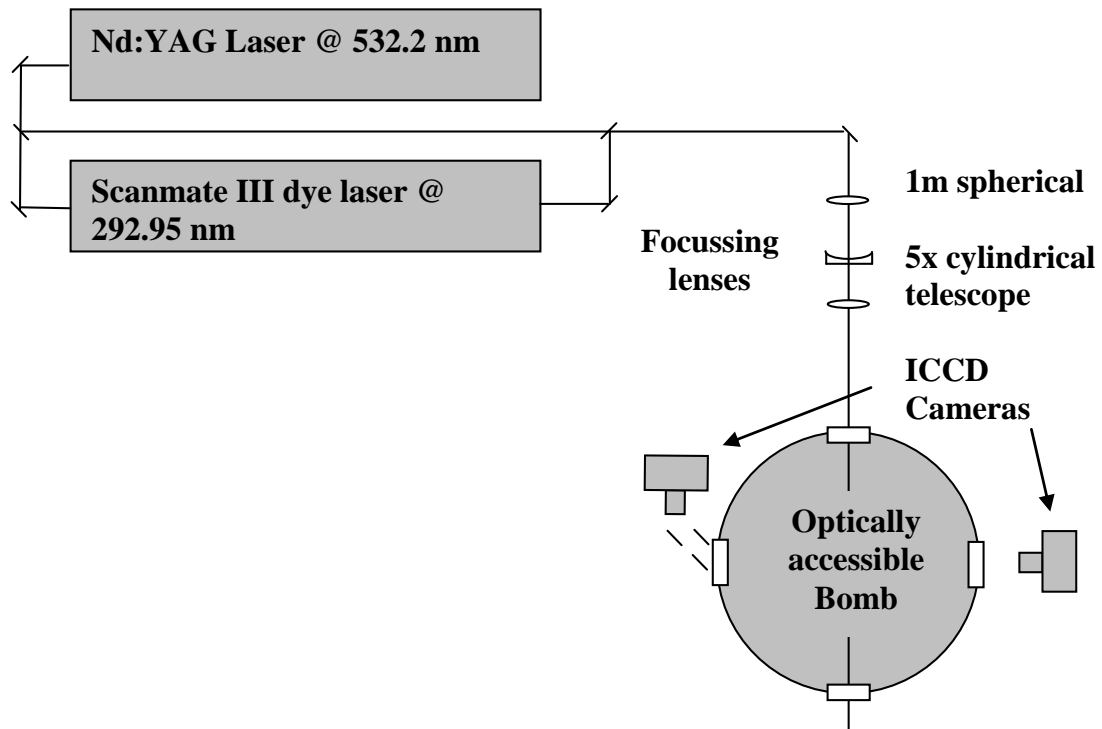
The second paper (Part 2) in the series will present a detailed length scale analysis of cellular flames and the soot structures obtained behind sooting explosion flames [10]. The length scale analysis demonstrates the presence of two length-scales in rich explosion flames, a long wavelength scale associated with the hydrodynamic instability (small wavenumber), and a short wavelength scale associated with the thermal-diffusive instability (large wavenumber). Soot formed behind rich explosion flames of critical equivalence ratio develops a honeycomb-like structure with a length scale that is co-incident with the large wavelength scale associated with the hydrodynamic instability.

Fully detailed modelling of these types of flames is presently intractable, due to the complexity of the rich flame chemistry and the three dimensional character of explosion flame instabilities. Therefore knowledge of the behaviour and structure of these flames is available only through the application of suitable diagnostics.

2. EXPERIMENTAL

2.1 The Leeds Combustion Bomb

The experimental layout of the lasers, optics and ICCD cameras relative to the Leeds Combustion Bomb is shown schematically in Figure 1.

Figure 1: Schematic of Experimental Layout

Spherical explosion flames were initiated with central laser ignition in the Leeds optically accessible bomb, described in Gillespie *et al* [22]. The bomb is a stainless steel spherical vessel of 39 cm internal diameter. It has six optically accessible ports of 15 cm diameter, and four high speed fans mounted at tetrahedral apexes for the generation of isotropic turbulence at the geometric centre of the vessel.

Combustion mixtures are prepared by initially pressurising the bomb to the desired partial air pressure, followed by manual injection of a pre-determined mass of fuel into

the bomb. The fuel is then stirred into the air with the fans. After mixing, the fans are turned off, and the total mixture pressure is checked for consistency. The initial mixture pressure, temperature and equivalence ratio are subject to absolute errors of $\delta P = \pm\ 0.1$ bar, $\delta T = \pm\ 5$ K and $\delta\phi\ = \pm\ 0.02$ respectively.

The initial mixture pressure and temperature were 2.0 ± 0.1 bar and 308 ± 5 K respectively. The iso-octane-air mixture equivalence ratio was varied from $\phi = 1.4$ to $\phi = 2.0$ in $\Delta\phi = 0.1$ steps until soot formation behind the flames was observed. Three explosions were performed at $\phi = 1.4$, one each at $\phi = 1.5, 1.6, 1.7, 1.8,$ and 1.9, and four explosions at $\phi = 2.0$. An expanding stoichiometric iso-octane-air flame of initial pressure 2.0 bar reaches a maximum pressure of 2.2 bar at a flame diameter of 100 mm. Therefore the early expansion of the flame in the bomb occurs at nearly isobaric conditions. The expanding flames were imaged using fast video shadowgraphy. Separately, simultaneous single shot OH fluorescence and Rayleigh scattering images were obtained at a flame diameter of approximately 90 mm – 100mm.

2.2 OH Laser Induced Fluorescence

A Spectra Physics Quanta Ray GCR-270 injection seeded Nd:YAG laser operating at 532 nm ($\mathrm{TEM_{00}}$ operation, 900 mJ per pulse, 7 ns duration, 10 Hz) was passed through a 50-50 beam splitter. The transmitted beam was employed to transversely pump a Lambda Physik Scanmate III dye laser, producing a pulsed dye laser beam at 565.90 nm. The pulsed dye laser beam was then frequency doubled to 282.95 nm, tuned to the $Q_1(6)$ line of the $(1 - 0)$ $A^2\Pi \leftarrow X^2\Pi$ transition in OH (pulse width 0.001 nm, pulse duration ~ 10 ns, pulse energy ~ 10 mJ). The fluorescence emission obtained from exciting the $Q_1(6)$ line is large, and weakly dependent on temperature over the range 1600 K – 2300 K (less than 5% variation from the mean).

The pulsed dye laser beam exiting the dye laser was then expanded through an inverted 3x Galilean telescope, and then combined with the 450 mJ/pulse 532 nm $\mathrm{TEM_{00}}$ laser beam obtained from the Nd:YAG laser, using a dichroic mirror. The inverted 3x Galilean telescope was employed to match the dye laser beam diameter to the Nd:YAG laser beam diameter, and to optically correct chromatic aberration occurring in the following laser sheet focussing optics.

The combined beams were then focussed using a 1 m focal length spherical lens and expanded through an inverted 5x cylindrical telescope, forming a 2-d pulsed laser sheet of 40 mm height and 0.2 mm width at the focus. The combined 2-d laser sheet was then directed through the optically accessible bomb through 12 cm high fused silica windows.

$0 - 0$ and $1 - 1$ fluorescence produced by the OH in the flame at 308 nm was imaged onto a 100 ns gated Princeton Instruments 512 x 512 pixel 12-bit ICCD camera, employing a 105 mm f4.5 Nikon uv lens. The on-resonance scattering at 282.95 nm was reflection filtered using three successive 50 mm diameter filtering mirrors. The three filtering mirrors used together produced an elastic scattering filtering factor of approximately 10^{-4}. A 56 mm x 56 mm square region, located 50 mm below the laser spark, was imaged (vertical image range 22 mm to 78 mm below laser spark). The transverse spatial resolution attained by the imaging system was 0.110 mm/pixel.

The $Q_1(6)$ line in the OH $A^2\Pi \leftarrow X^2\Pi$ transition excited by the 2-d dye laser sheet at 282.95 nm was determined to be partially saturated ($I/I_{Sat} \approx 2.0$) by plotting a saturation calibration curve using a Bunsen flame at the centre of the bomb at atmospheric pressure. The flame measurements reported here were conducted at a pressure of 2.0 bar. The laser saturation spectral flux density is expressed as

$$I_{sat}(\nu) = c\,\frac{\sum\limits_{f} A_{fi} + Q_{fi}}{g_i B_{fi} + g_f B_{if}} = c\,\frac{\sum\limits_{finalstates} A_{fi} + \sum\limits_{species} c_i \sigma_i v_i}{g_i B_{fi} + g_f B_{if}} \qquad (2.2.1)$$

where c is the speed of light, A_{fi} and Q_{fi} are the Einstein coefficients for spontaneous emission and molecular quenching lifetime respectively, B_{fi} and B_{if} are the Einstein coefficients for stimulated emission and absorption respectively, g_i and g_f are the respective degeneracy of the initial and final states, and c_i, σ_i and v_i are the i'th gas species molecular density, quenching cross-section and relative molecular velocity respectively. Raising the operating pressure in the bomb affects the saturation laser spectral flux density predominantly through the molecular density term that appears in the quenching lifetime. As a result of the molecular quenching term dominating the numerator in Equation (2.2.1), raising the bomb pressure from 1 bar to 2 bar causes the

saturation spectral flux density to approximately double. Therefore during the 2 bar combustion experiments $I/I_{Sat}(2 \text{ bar}) \approx 1$.

The local dye laser sheet flux density was measured in the interrogation region near the centre of the bomb. This was obtained by subtracting a mean background image from a mean constant density OH image obtained from equilibrium OH occurring naturally in the hot combustion gas following a flame front. If B_{ij} and S_{ij} denote the signal intensities from the mean background image and the averaged constant OH calibration image measured on the CCD array respectively, then the local laser flux density profile L_{ij} can be expressed as

$$L_{ij} = S_{ij} - B_{ij} \qquad (2.2.2)$$

Employing a simple top hat laser profile enabled the computation of a partial saturation laser calibration image, which takes the form

$$C_{ij} = \frac{L_{ij}}{1 + L_{ij}/L_{Sat}} \qquad (2.2.3)$$

Denoting the raw flame OH data images by D_{ij}, the processed OH images were obtained through the determination of

$$P_{ij} = \frac{D_{ij} - B_{ij}}{C_{ij}} = \frac{D_{ij} - B_{ij}}{\dfrac{L_{ij}}{1 + L_{ij}/L_{Sat}}} \qquad (2.2.4)$$

The top hat assumption produces a spatially dependent error in the measurement of local OH concentration of approximately 7 % magnitude in the measurement region, a result of the varying impact of major species dependent collision quenching of the excited OH molecules in the wings of the laser focus [23].

There are a number of contributions to the error associated with single shot measurement of OH concentration. The top hat longitudinal laser profile employed above introduces approximately 7 % error to the local estimate of OH concentration, a

consequence of the spatially varying contribution of quenched fluorescence in the wings of the laser pulse. The dye laser operates with an rms pulse energy fluctuation of approximately 5 %. Shot-to-shot variations in laser profile produce a variation from the mean of approximately 5 % magnitude. Laser pixel to pixel optical shot noise has a magnitude of approximately 8 % of equilibrium OH signal at $\phi = 1.4$, rising to approximately 17 % of equilibrium OH signal at $\phi = 2.0$. The contribution of optical shot noise to the measurement error can be reduced by summing (binning) the signal from adjacent pixels, and then analysing the distribution of locally binned pixels. The various sources of measurement error discussed above produce an overall measurement error in OH concentration of approximately 10 %.

The signal intensity from the equilibrium region of a processed OH flame data image obtained from a spherically expanding, stoichiometric, 2 bar methane-air laminar explosion flame was compared with the equilibrium OH concentration obtained from a previously computed, 1-d, stoichiometric, 2 bar spherically expanding, methane-air flame profile of the same radius (using RUN-1DL) in order to quantify the equilibrium OH signal in terms of OH concentration [24]. RUN-1DL is the Fortran program contained in the COSILAB suite that is employed to compute 1-d spherical explosion flame profiles. The iso-octane-air OH flame data was then quantified by a comparison between the computed 1-d flame equilibrium OH and the equilibrium OH concentration calculated using the Olikara-Borman equilibrium chemistry program suite [25] for both methane-air combustion and iso-octane-air combustion. The Olikara-Borman equilibrium programs are a suite of Fortran programs that perform a standard chemical equilibrium and adiabatic flame temperature calculation resulting from arbitrary hydrocarbon combustion for constant volume and constant pressure systems.

2.3 Rayleigh Scattering

The co-incident 282.95 nm and 532 nm laser sheets were directed through quartz windows into and out of the bomb, achieving a co-incident longitudinal focus at the bomb centre. The 532 nm elastic Rayleigh scattering obtained from the unburned and burned mixture across the flame-front in the bomb centre was imaged through a narrow-band 532 nm filter, onto a 100 ns gated 576 x 384 pixel 16-bit Princeton Instruments ICCD camera using a 50 mm f1.2 Nikon lens coupled to a Nikon 2x teleconverter,

producing a 100 mm f2.4 lens. A 64.5 mm wide x 43 mm high rectangular region, located 50 mm below the laser spark, was imaged (vertical image range 28.5 mm to 71.5 mm below laser spark). The transverse spatial resolution attained by the imaging system was 0.112 mm/pixel.

A mean Rayleigh background image was obtained from the interior of the bomb after a repeated evacuation of the bomb using a vacuum pump. One hundred elastic scattering background images were accumulated on the ICCD camera to produce the mean background image, denoted by X_{ij}. The mean background image was then subtracted from the raw data images (denoted by T_{ij}) to produce the background-subtracted raw data images (denoted by Q_{ij}).

A raw laser calibration image was then obtained through accumulating multiple Rayleigh scattering images obtained from the bomb filled with filtered air (denoted by F_{ij}). The processed mean laser calibration image was then obtained through the subtraction of the mean background image from the mean laser calibration image (denoted by I_{ij}). The final processed data images (denoted by R_{ij}) were obtained by dividing the background-subtracted raw data images by the processed mean laser calibration image. These are expressed in the form

$$R_{ij} = \frac{Q_{ij}}{I_{ij}} = \frac{T_{ij} - X_{ij}}{F_{ij} - X_{ij}} \qquad (2.3.1)$$

If the local pressure and composition of the unburned mixture and the burned mixture are known, together with the temperature of the unburned mixture, then the Rayleigh scattering signal can be employed to determine the temperature of the burned gas. This can be expressed in the form

$$T_{burnedgas} = \frac{R_{unburnedgas}T_{unburnedgas}\left[\sum_i x_i\left(\frac{d\sigma}{d\Omega}\right)_i\right]_{burnedgas}}{R_{burnedgas}\left[\sum_i x_i\left(\frac{d\sigma}{d\Omega}\right)_i\right]_{unburnedgas}}, \qquad (2.3.2)$$

where R represents the local Rayleigh scattering signal intensity, $\sum_i x_i\left(\frac{d\sigma}{d\Omega}\right)_i$ represents the local mean Rayleigh scattering cross section, and T represents the local temperature.

There are a number of contributions to the error associated with single shot Rayleigh scattering measurement. Shot-to-shot variations in laser profile can cause a local relative variation in energy flux density to the mean energy flux density of up to 20%. The magnitude of this effect can be reduced through local averaging of signal intensity. However, this effect remains the largest contributor to the error in single shot Rayleigh scattering temperature measurement, through the variation in the processed signal ratio $\frac{R_{unburned}}{R_{burned}}$ in Equation 2.3.2 above.

The Rayleigh scattering cross-sections are quoted with a precision of 99 % or better. There appear to be few measurements of the Rayleigh scattering cross-section of iso-octane, the most reliable of which is referenced here [28]. Pixel to pixel optical shot noise has a magnitude of approximately 8 % of mean intensity in the unburned mixture, rising to approximately 20 % of mean intensity in the burned mixture. The contribution of optical shot noise to the measurement error can be reduced by summing (binning) the signal intensity from adjacent pixels, and then analysing the statistical distribution of the signal intensities obtained from locally binned pixels.
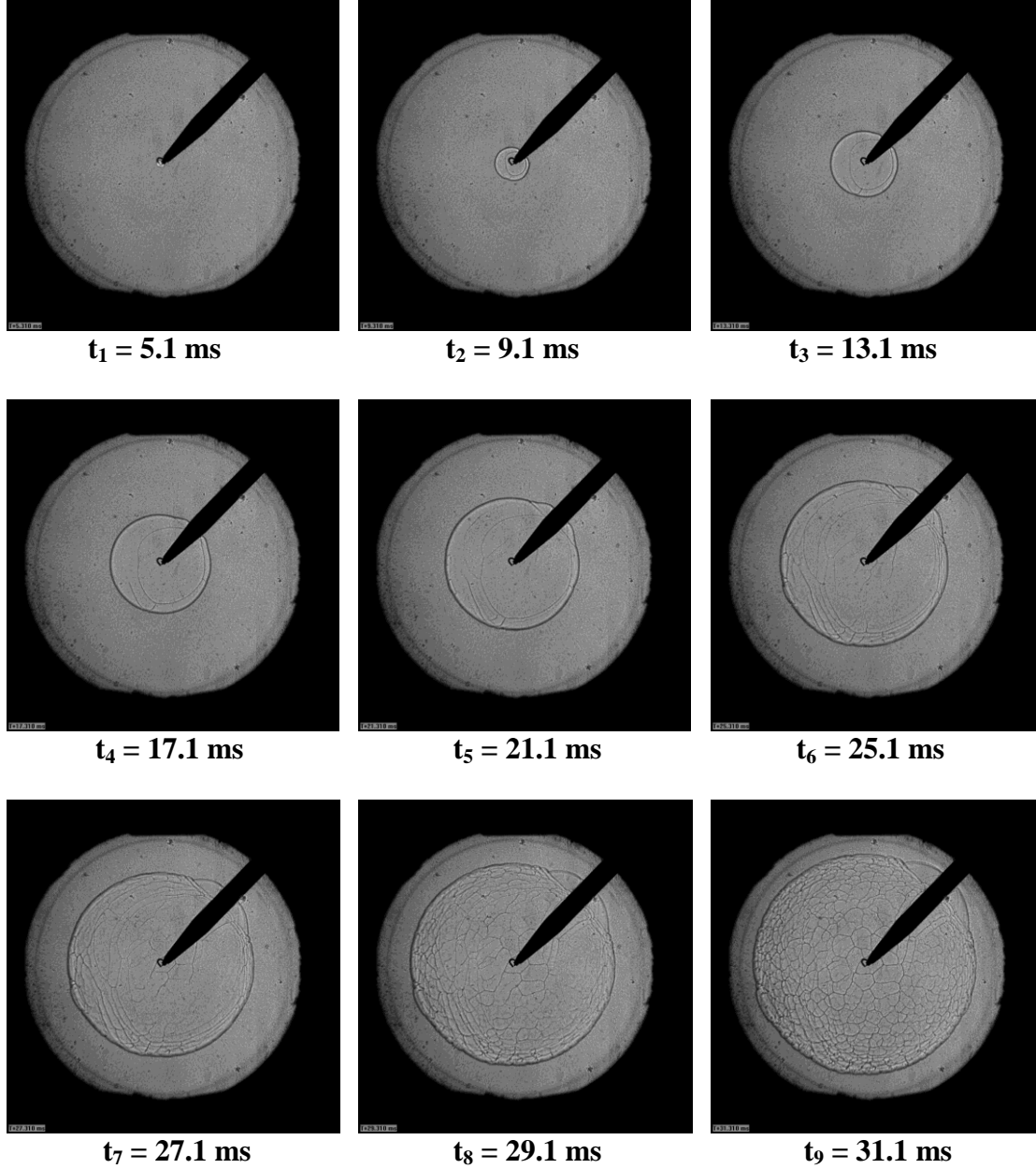
2.4 High-Speed Shadowgraph Imaging

High speed shadowgraph images were obtained from a high speed CMOS camera (Photosonics Phantom 9) operating at 2 kHz frame rate. Spherical explosion flames were initiated in the Leeds bomb using spark ignition. The iso-octane-air mixtures were prepared at 2.0 ± 0.1 bar and 308 ± 5 K respectively. Details of the experimental layout can be obtained from reference [26].

3. RESULTS

3.1 Dynamics and Structure of the 2 bar, $\phi = 1.4$ Iso-octane-Air Explosion Flame

Figure 2 shows successive shadowgraph images of a 2 bar, $\phi = 1.4$, spherically expanding iso-octane-air flame. The diameter of the viewing window is 15.0 cm. The first image presented was obtained at 5.1 ms after the ignition pulse. The following five
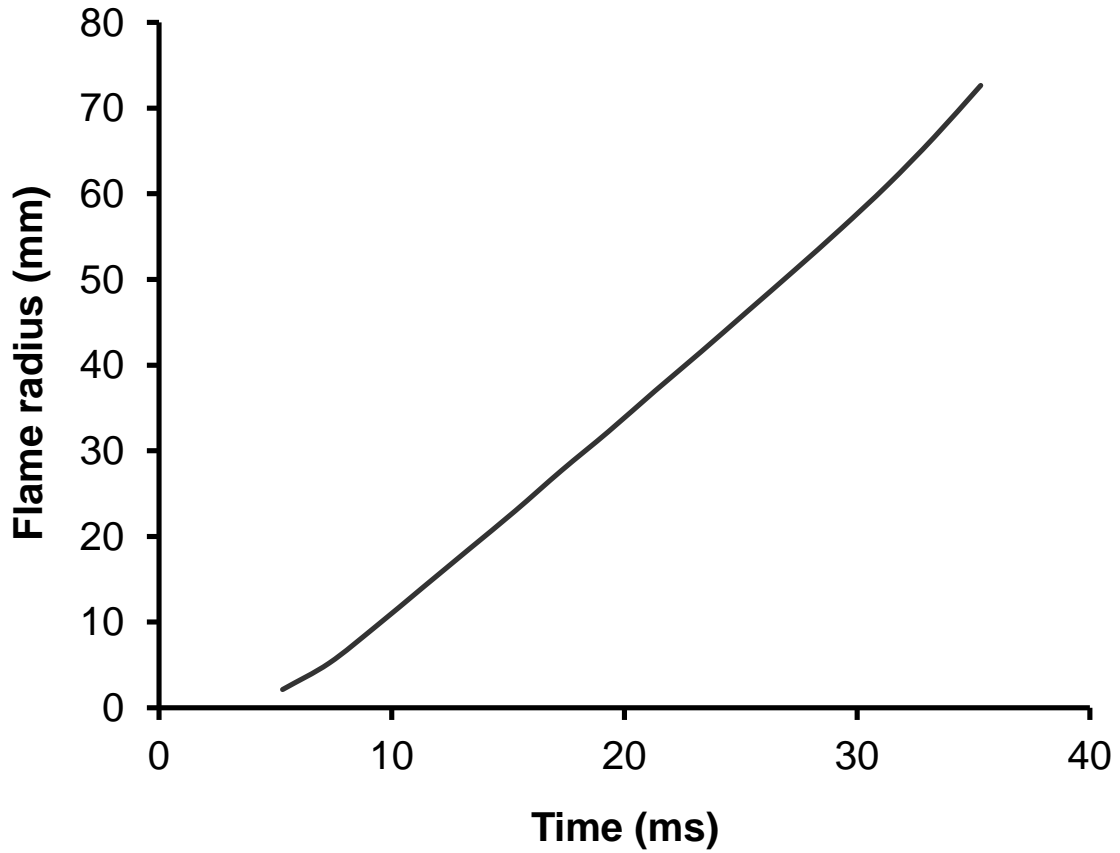
images are shown at 4 ms intervals, followed by the last three images shown at 2 ms intervals. The critical radius for the onset of cellularity is chosen to be consistent with Jomaas *et al* [3], when the cellularity is observed to spread rapidly over the entire surface. This is observed to begin at $t_7 = 27.1$ ms (frame 7 of Figure 2), when the flame diameter is approximately 95 mm.

Figure 2: Shadowgraph images of a 2 bar, $\phi = 1.4$ iso-octane-air explosion flame. (Window diameter = 15.0 cm)

Figure 3 shows a graph of expanding flame radius with time, obtained from the explosion flame shown in Figure 2. The rate of radial expansion of the flame is nearly

13

constant over the radius range 10 mm < r < 50 mm, corresponding to a flame radial expansion velocity of 2.35 ± 0.05 m/s. The radial expansion velocity begins to increase for r > 50 mm (frame 8 of Figure 2). This corresponds to the approximate flame radius (critical Peclet number Pe_c) when the cellularity spreads over the entire flame surface. The radial expansion velocity increases to 3.02 ± 0.05 m/s at a radius of 70 mm. This observation is consistent with other measurements [27].

Figure 3: Graph of Radial Flame Expansion (2 bar, ϕ = 1.4 iso-octane-air explosion flame) versus Time.

Figures 4 (a), (b) and (c) show a relative OH concentration field, a processed Rayleigh image, and a Shadowgraph image obtained from a ϕ = 1.4 iso-octane-air flame with a radius of approximately 48 mm (~ frame 7 of Figure 2) respectively. The flame is travelling downwards, with the burned gas at the top of the images and the unburned

14

mixture at the bottom of the images. The flame surface is made up of a number of discrete convex flame cells (crests) containing super-equilibrium OH concentration, bounded by concave flame cusps (troughs) with very large negative curvature at their base. A number of flame cusps are explicitly identified in Figure 4 (a). The local OH concentration is reduced at the base of the cusps, suggesting a relative reduction in the local rate of fuel oxidation. This is a consequence of the impact of negative stretch on the local dynamic behaviour and structure of the flame. The OH concentration behind the flame cells and the cusps rapidly attains steady-state levels (approximately 12 mm behind the flame front). This steady-state concentration is the local equilibrium OH concentration.

The Rayleigh image (Figure 4 (b)) has a very similar flame edge to that of the OH concentration image. There is a sharp transition between the cold dense unburned mixture ahead of the flame front, and the hot combustion products formed behind the flame front. Mie scattering from particles in the unburned mixture ahead of the flame front are clearly visible. The boundary between hot and cold gas across the cells and the cusps appear similar. Furthermore, Rayleigh scattering behind the flame cells and the cusps is remarkably uniform, suggesting high temperature uniformity, a consequence of a high rate of thermal diffusion resulting in local thermal equilibrium. The flame cells have a distribution of physical sizes between 2 mm and 5 mm, in agreement with the observations of Bradley *et al* [1].

Figures 5 (a) and (b) show normalised OH concentration profiles and normalised Rayleigh scattering profiles across a convex cell and across an adjacent cusp as identified in Figure 4 (a). Both OH concentration and Rayleigh scattering intensity are normalised with respect to their equilibrium values in the burned gas. The normalised OH concentration profile is shown in black, while the normalised Rayleigh scattering profile is shown in grey. The horizontal axis measures distance relative to the origin, which is located arbitrarily in the burned gas behind the flame front. The preheat zone for both flame cells and flame troughs is identified from the normalised Rayleigh scattering profiles as the narrow region where the curve drops from the large value
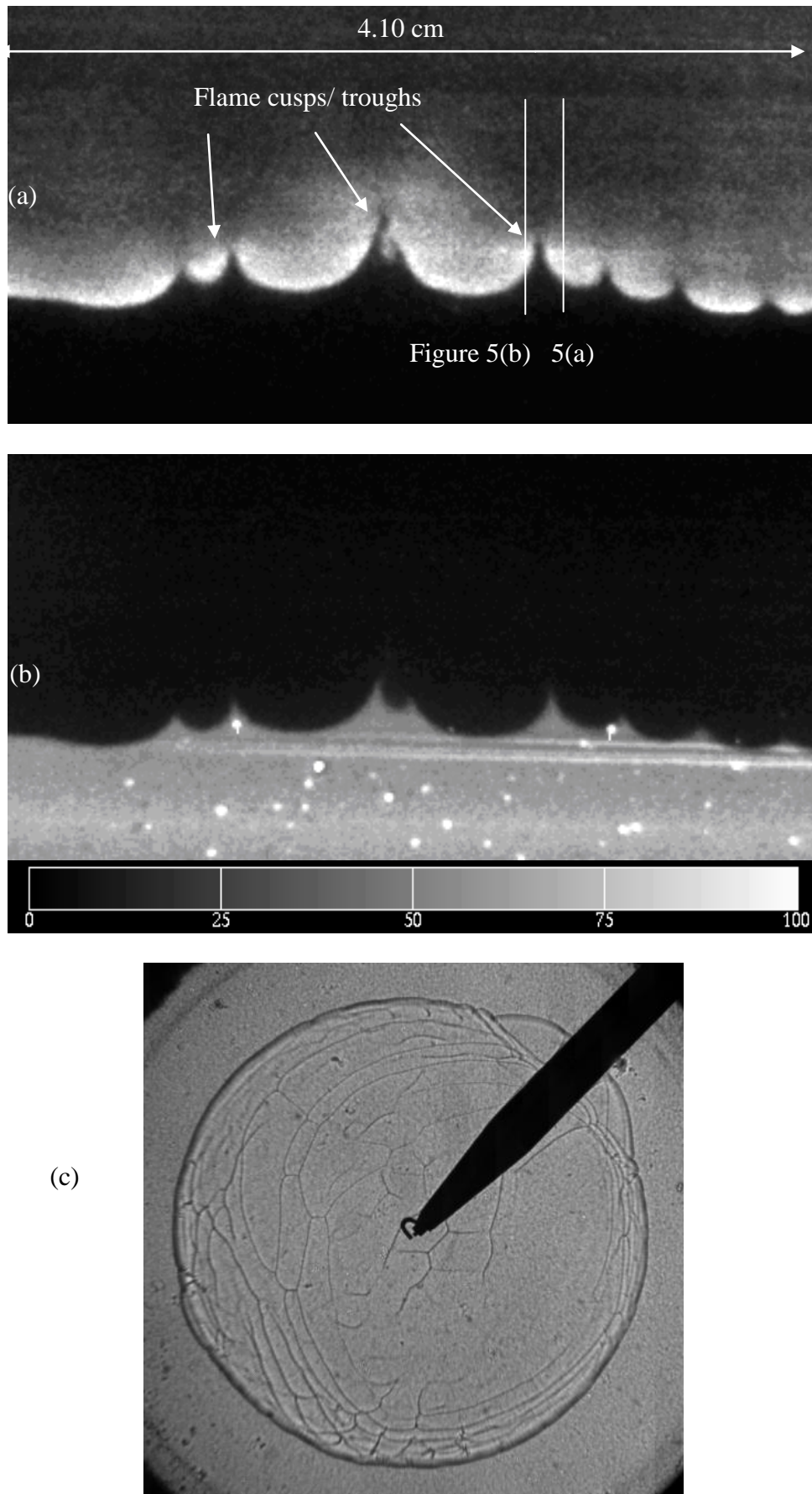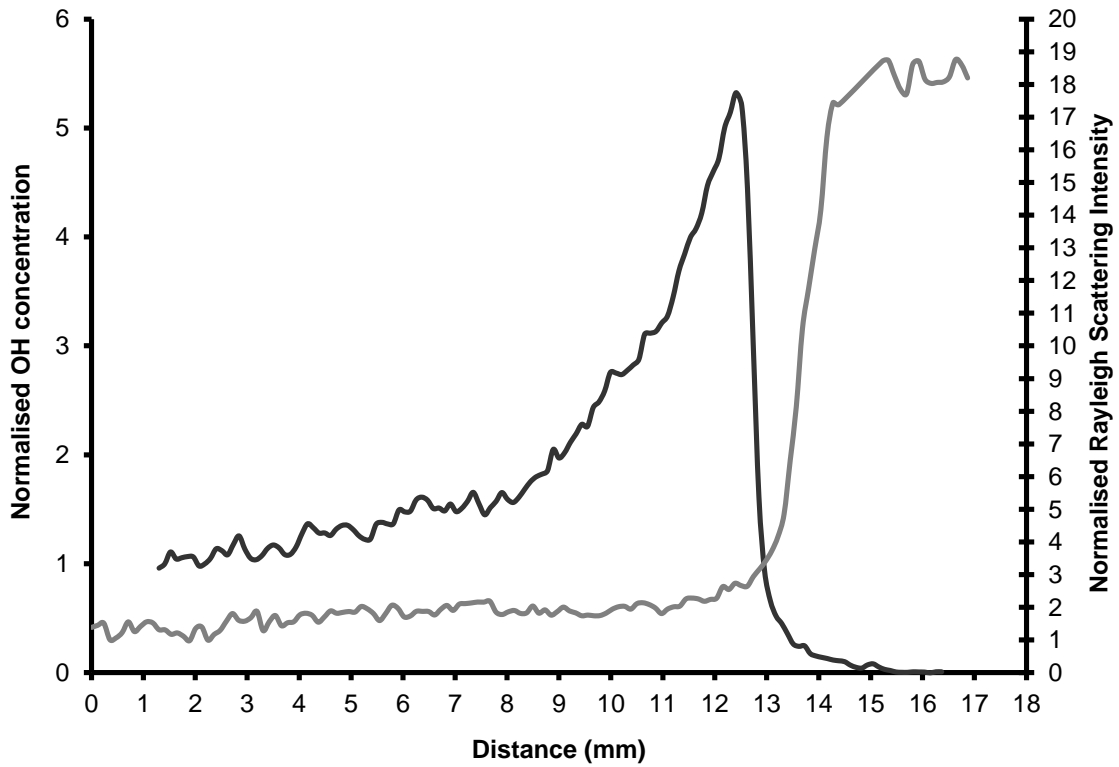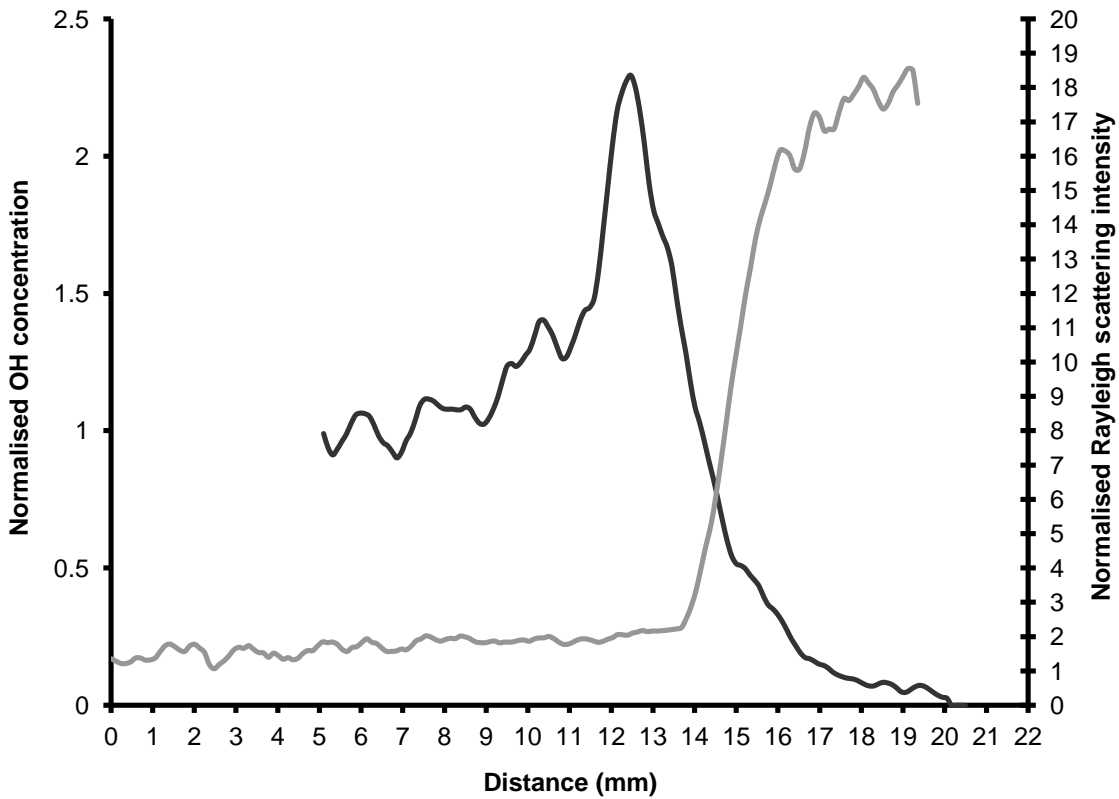
Figure 4: (a) OH concentration, (b) Rayleigh scattering, (c) Shadowgraph image of a 2 bar, $\phi = 1.4$ iso-octane-air explosion flame (diameter ~ 95 mm).

Figure 5: (a) Graph of normalised OH concentration and Rayleigh scattering intensity across a convex flame cell as a function of position.

Figure 5: (b) Graph of normalised OH concentration and Rayleigh scattering intensity across a concave flame trough as a function of position.

associated with the low temperature unburned mixture, to the low value associated with the high temperature gas.

The preheat zone thickness associated with a typical flame cell is estimated from Figure 5 (a) to be approximately 1.0 mm. The corresponding preheat zone thickness associated with one of the flame troughs is estimated from Figure 5 (b) to be approximately 2.4 mm.

The flame reaction zone in convex flame cells and concave flame troughs is identified by the region in the neighbourhood of the maximum value of the relative OH concentration. In both Figure 5 (a) and 5 (b), this is observed to occur as the Rayleigh scattering profile flattens out on the left hand side of the preheat zone. Diffusion of OH radicals into the preheat zone can be observed in both graphs constituting Figure 5.

3.2 General Properties of the 2 bar, Rich, Cellular Iso-octane-Air Explosion Flames

Figure 6 shows a graph of normalised equilibrium OH concentration as a function of equivalence ratio in the range $\phi = 1.4$ to $\phi = 2.0$. The data points with error bars represent the normalised equilibrium OH concentrations obtained from the OH fluorescence experiments in the bomb, while the continuous line shows normalised theoretical equilibrium OH concentrations obtained from calculations [23, 24]. The normalised experimental equilibrium OH concentration is set equal to the normalised theoretical equilibrium OH concentration at $\phi = 1.4$. The error bars represent one standard deviation in the estimate of normalised OH concentration and equivalence ratio. In general, good agreement is attained between the normalised experimental equilibrium OH concentrations and the normalised calculated equilibrium OH concentrations for all mixtures, except for $\phi = 1.7$. It appears that the true mixture strength of the $\phi = 1.7$ point is approximately $\phi = 1.74$, slightly outside the single standard deviation error bar.

Figure 7 shows a graph of the ratio of the mean super-equilibrium OH concentration in the oxidising cells, to the equilibrium OH concentration, as a function of equivalence ratio, over the equivalence ratio range $\phi = 1.4$ to $\phi = 2.0$. The vertical error bars represent the range of variation in the determination of peak to equilibrium OH

18

concentration ratio. These error bars are representative of the range of peak OH concentration found in all of the cells present in the OH image data as a function of equivalence ratio, plus the error estimate in the measurement of the OH concentration. The horizontal error bars represent one standard deviation estimate of error in the measurement of mixture equivalence ratio.
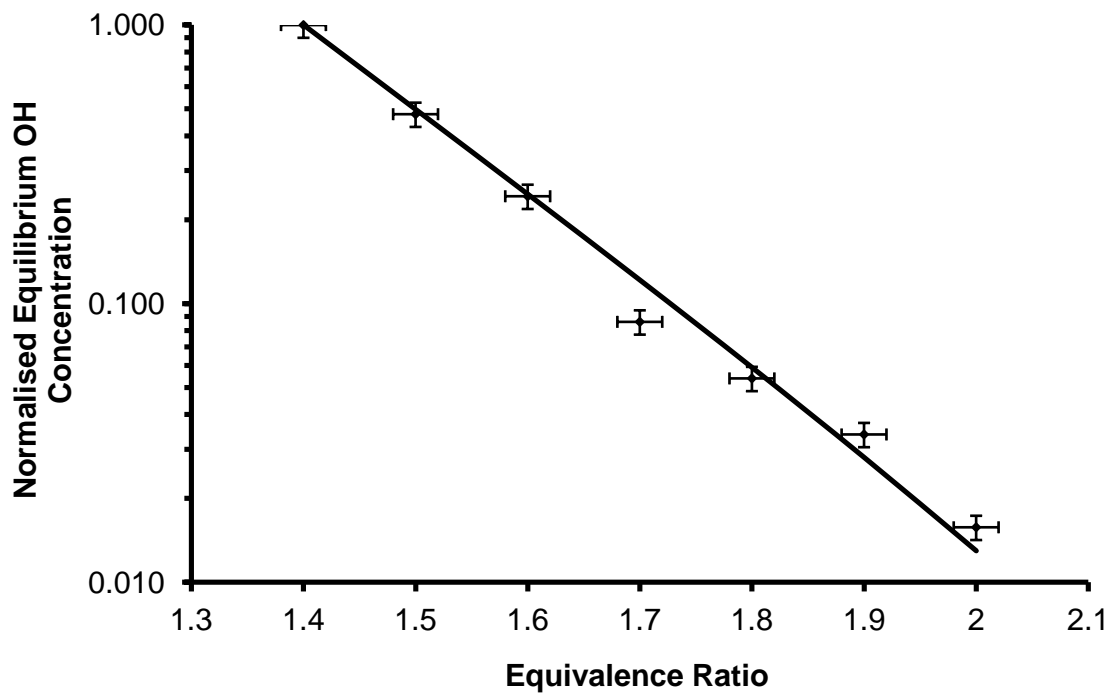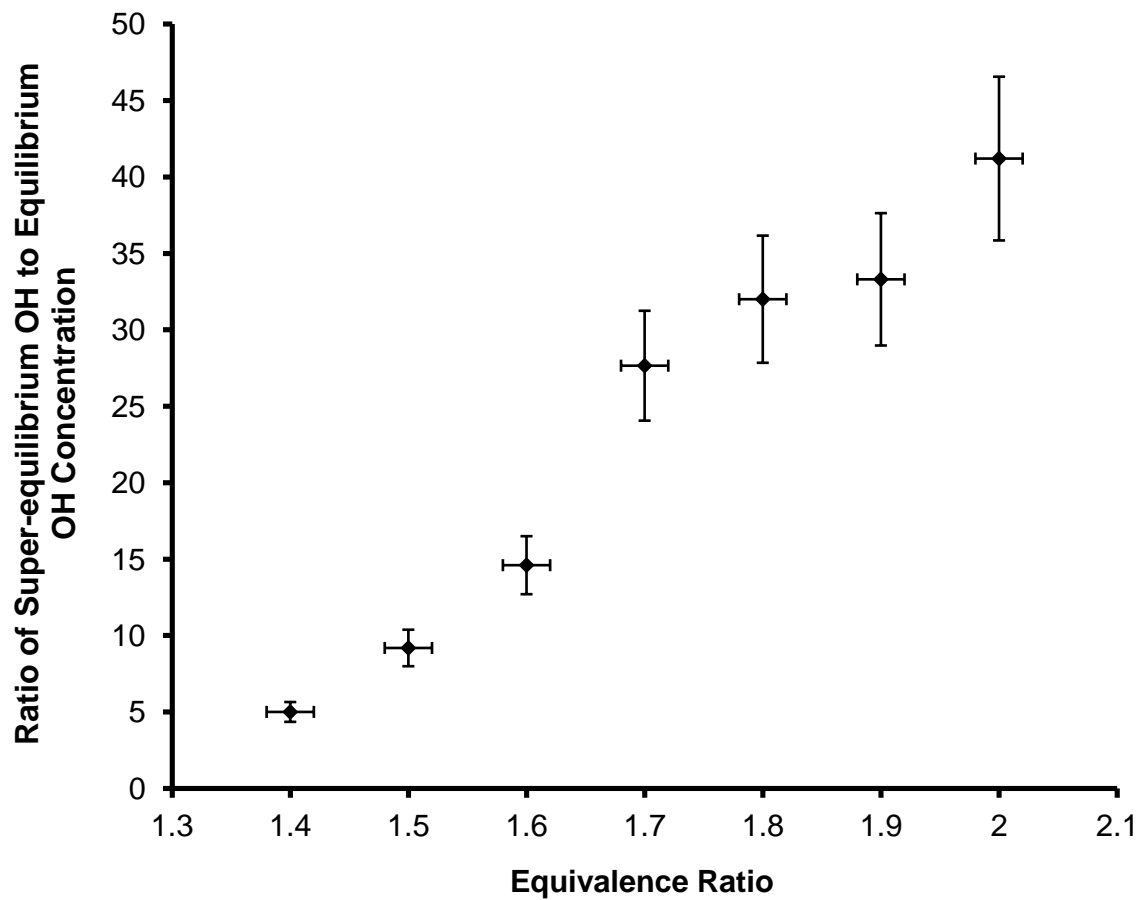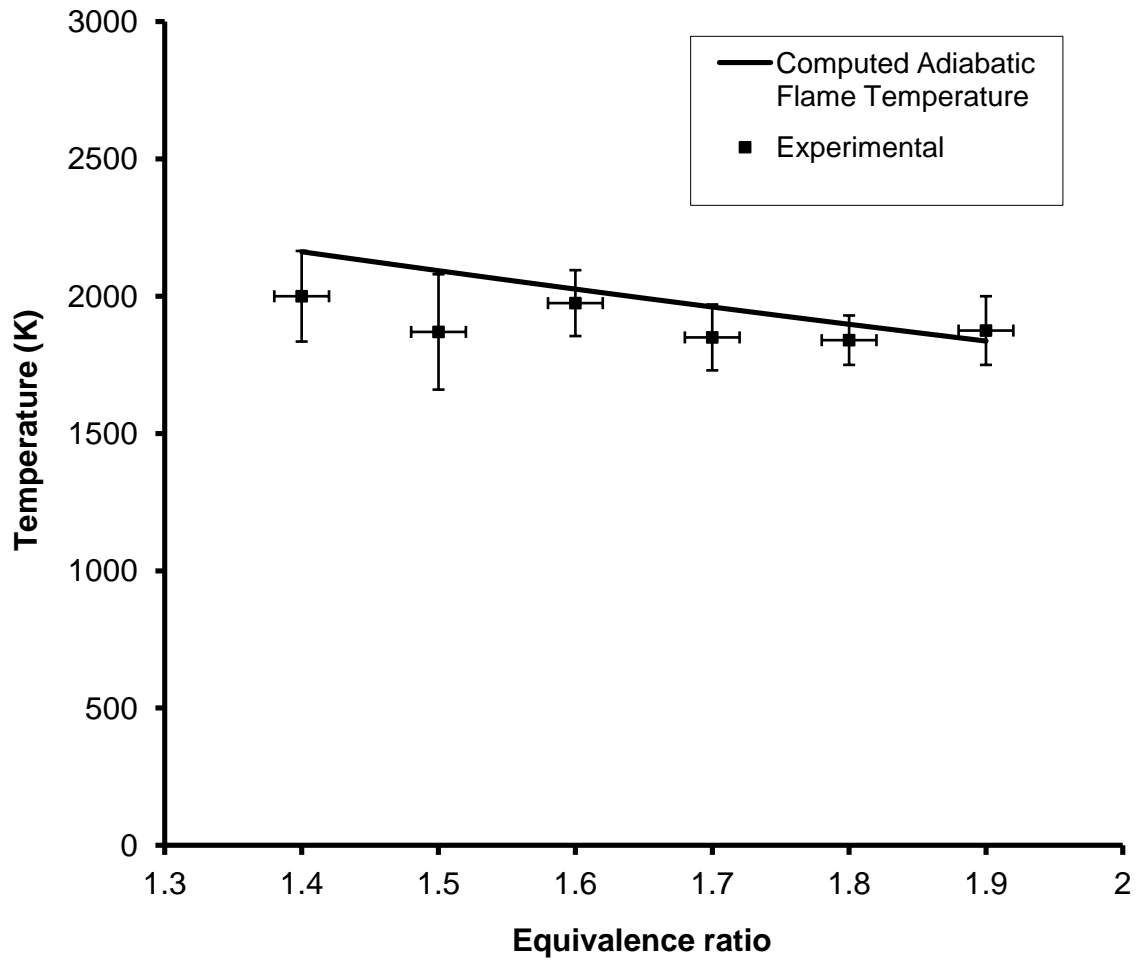

Figure 6: Graph of normalised equilibrium OH concentration as a function of equivalence ratio.

Combustion gas temperatures have been estimated from the Rayleigh scattering data in the burned gas, over the equivalence ratio range $\phi = 1.4$ to $\phi = 1.9$, assuming the burned gas has achieved equilibrium composition. Relevant Rayleigh scattering cross-sections have been obtained from Koch *et al* [28] and Long [29]. Figure 8 shows the comparison between the experimentally obtained burned gas temperatures and the computationally obtained adiabatic flame temperatures. The temperature data points with error bars represent the experimentally obtained burned gas temperatures derived from the processed Rayleigh images. The continuous curve represents the computationally determined adiabatic flame temperature as a function of equivalence ratio.

The error bars represent one standard deviation in the estimate of equivalence ratio, which is ± 0.02 absolute, and 95 % confidence interval relative to the local mean in the temperature. All six data points are in agreement with the theoretical adiabatic flame temperatures within error limits. However, the experimental burned gas temperature trend is observed to be lower than the corresponding predicted adiabatic flame temperatures. This might be expected to occur as a result of radiation heat loss from the burned gas.
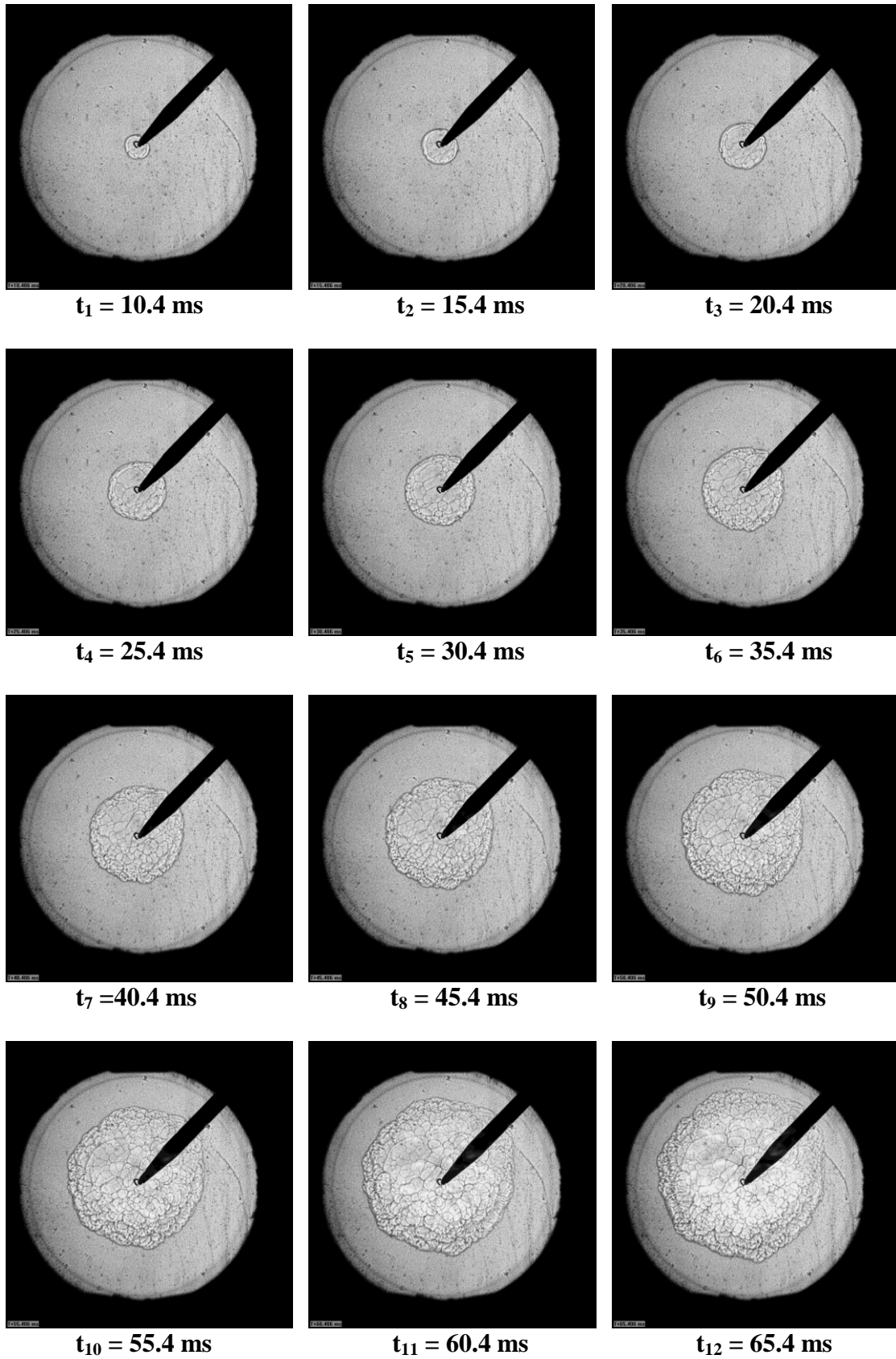

Figure 7: Graph of the ratio of super-equilibrium OH concentration to equilibrium OH concentration as a function of equivalence ratio.

Figure 8: Graph of burned gas temperature as a function of equivalence ratio.

3.3 Dynamics and Structure of the 2 bar, $\phi = 1.8$ Iso-octane-Air Laminar Explosion Flame
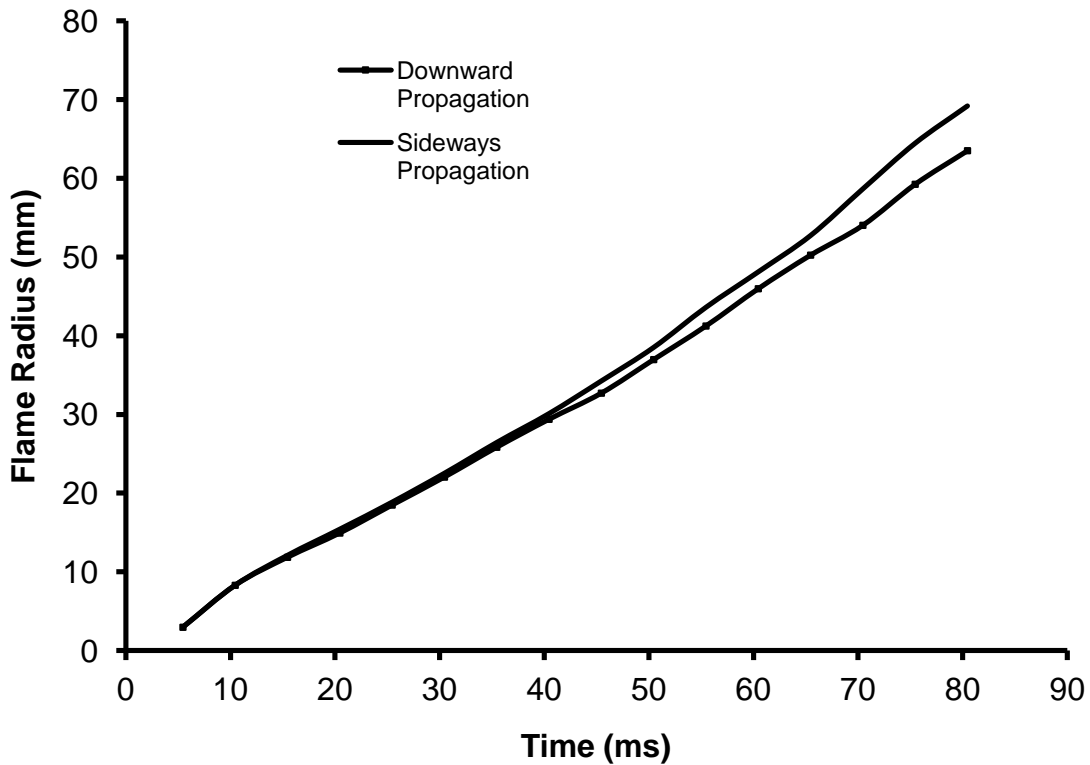
Figure 9 shows shadowgraph images of a 2 bar, $\phi = 1.8$ (C/O = 0.576) spherically expanding iso-octane-air explosion flame. The first image presented was obtained at 10.4 ms after the ignition pulse. The following images are shown at 5 ms intervals. Flame cellularity is observed to begin at $t \sim 20$ ms (frame 3 of Figure 9), when the flame diameter is approximately 30 mm. The flame is buoyant, which causes the upper surface to expand with a larger radial expansion velocity than the lower surface (i.e. the centre of mass of burned gas rises with time).
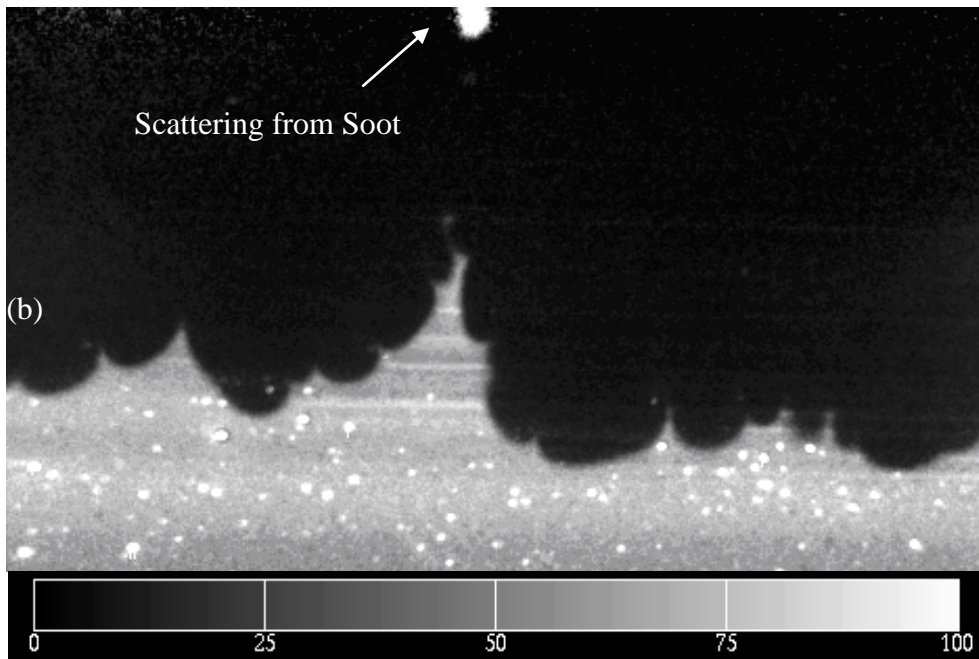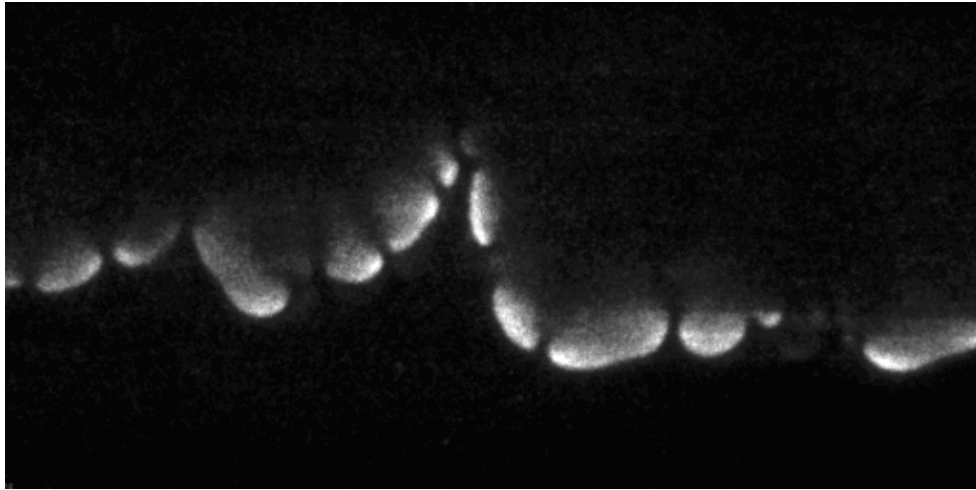
Figure 9: Shadowgraph images of a 2 bar, $\phi = 1.8$ iso-octane-air explosion flame (window diameter = 15.0 cm).
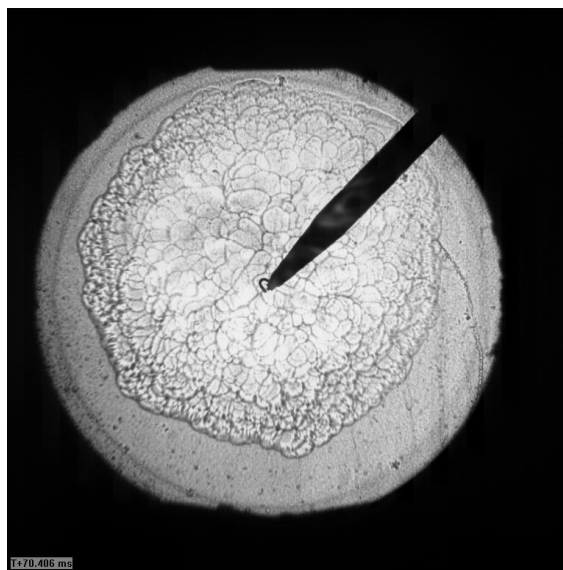
Figure 10 shows a graph of expanding flame radius with time, obtained from the $\phi = 1.8$ flame shown in Figure 9. The smooth curve corresponds to the plot of mean radial expansion sideways versus time, while the data curve with points corresponds to the plot of radial expansion downwards versus time. The difference between the two plots demonstrates the effect of buoyancy on the expanding flame surface. The rate of radial expansion sideways and downwards is nearly constant over the radius range 10 mm < r < 75 mm. The downward radial expansion observable in Figure 9 and 10 corresponds to a flame expansion velocity of 0.79 ± 0.03 m/s.

Figure 10: Graph of Radial Flame Expansion (2 bar, $\phi = 1.8$ iso-octane-air explosion flame) versus Time.

In image (b): Scattering from Soot

Figure 11: (a) OH concentration, (b) Rayleigh scattering, (c) Shadowgraph image of a 2 bar, ϕ = 1.8 iso-octane-air explosion flame (diameter ~ 100 mm).
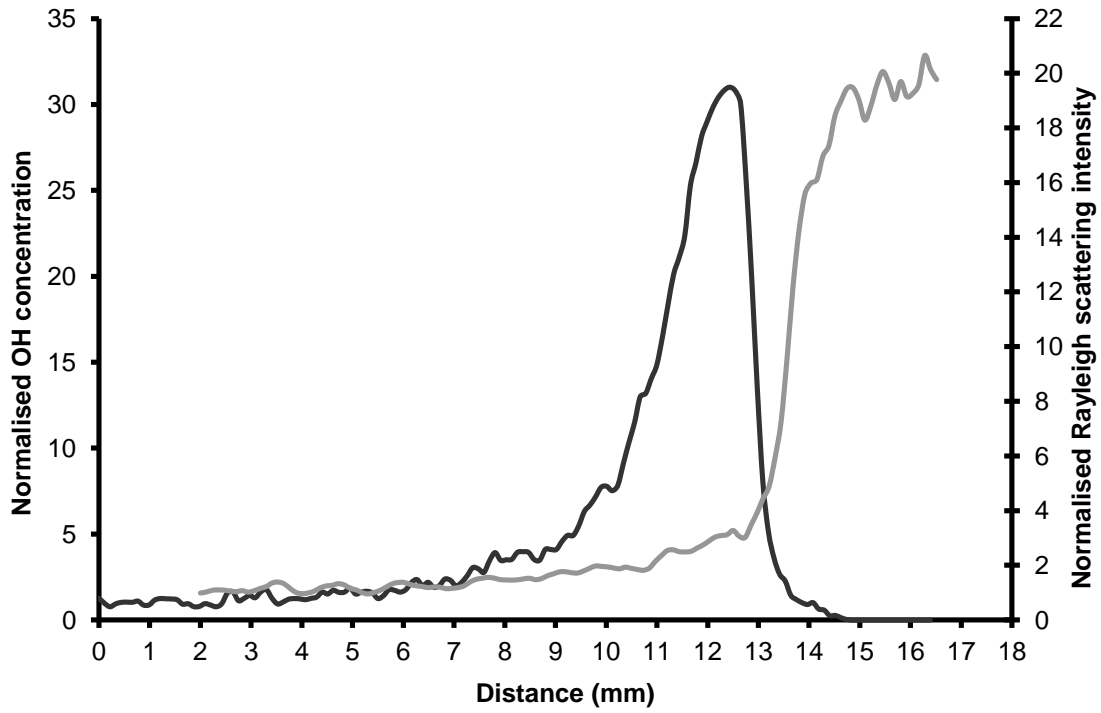
Figures 11 (a), (b) and (c) show a processed OH concentration field, a processed Rayleigh scattering image, and a shadowgraph image obtained from a ϕ = 1.8 iso-octane-air flame with a radius of approximately 52 mm. The cell sizes observed from this data are smaller (1 mm to 3 mm) than those observed in the ϕ = 1.4 data, and the cells are completely separated from each other. The Rayleigh image shows that the flame edge looks similar to that of the ϕ = 1.4 data, with most of the surface having positive curvature separated by cusps having large negative curvature.

Figures 11 (a) and (b) reveal some deep cracks containing a number of cells along the converging surfaces. This suggests the existence of two simultaneous, decoupled length scales, a short wavelength cellularity associated with the thermal diffusive instability, and a longer wavelength cellularity associated with the Darrieus-Landau hydrodynamic instability [8, 10].
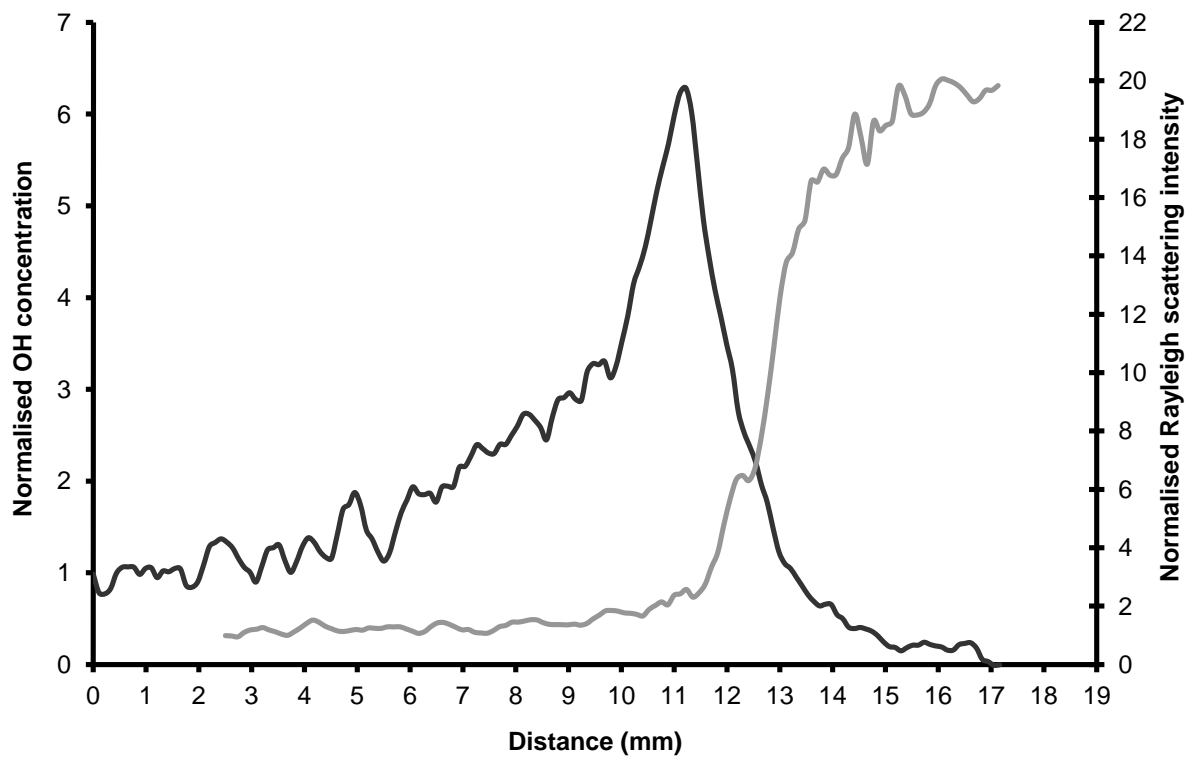
This equivalence ratio (ϕ = 1.8, C/O = 0.576) marks the critical equivalence ratio for the incipient formation of soot, in agreement with the findings of Tate [14], and Lockett [10]. High intensity elastic scattering from soot can be observed at the base of the deepest crack observable in Figure 11 (b). The soot is observed to form behind deep flame cusps (cracks). These flame cracks are believed to be a result of the large length-scale cellularity arising from the Darrieus-Landau hydrodynamic instability interacting with the short length-scale cellularity resulting from the thermal-diffusive instability.

Shadowgraph image frames 10 – 12 of Figure 9 are subject to white light contamination. This optical contamination is the result of broad-band grey body radiation emitted from soot formed behind the flame.

Figures 12 (a) and (b) show normalised OH concentration profiles and normalised Rayleigh scattering profiles across an oxidising cell and across a cusp as identified in Figure 11 (a). Both OH concentration and Rayleigh scattering intensity are normalised with respect to their equilibrium values in the burned gas. The normalised OH concentration profile is shown in black, while the normalised Rayleigh scattering profile is shown in grey. The horizontal axis measures distance relative to the origin, which is located in the burned gas behind the flame front. The preheat zone for both flame cells and flame troughs is identified from the normalised Rayleigh scattering profiles as the
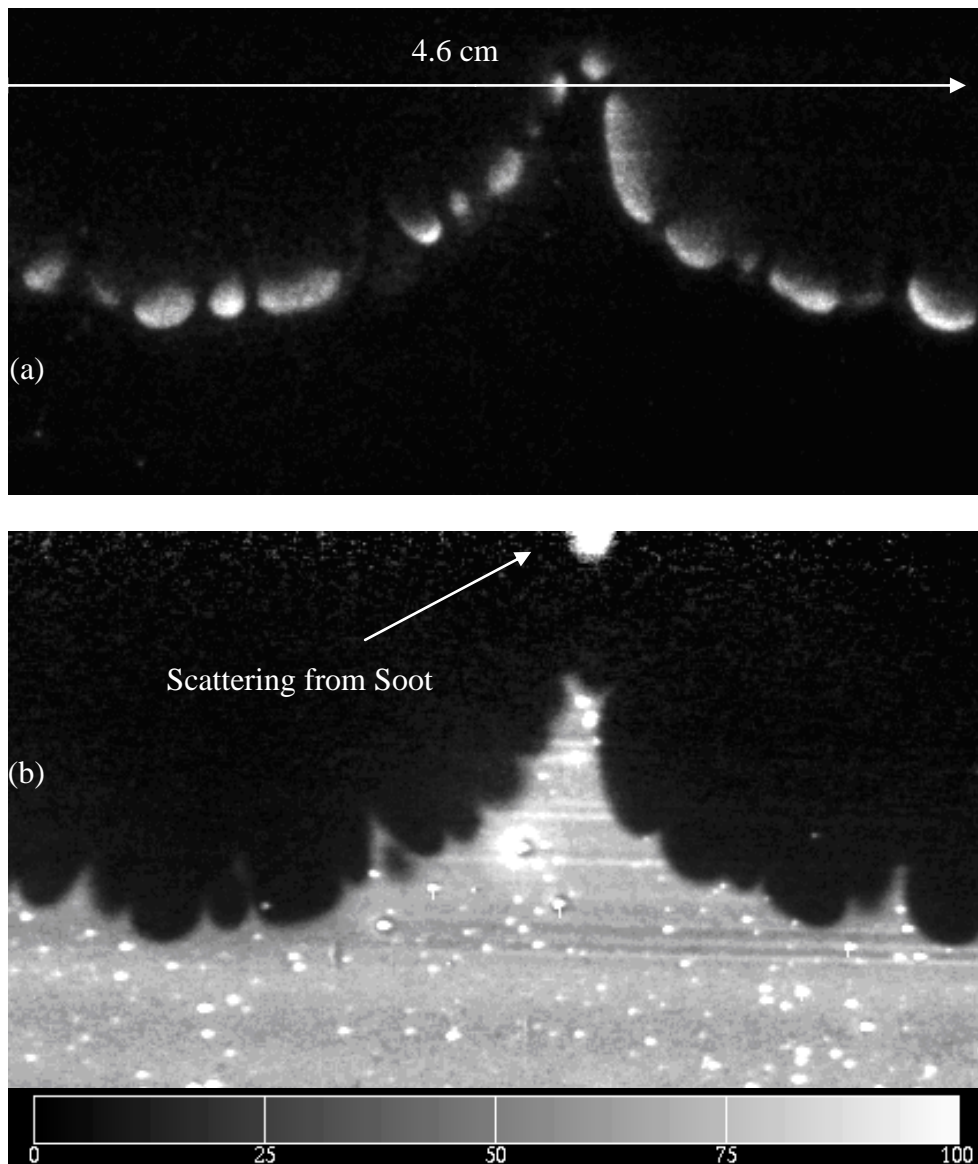
Figure 12: (a) Graph of normalised OH concentration and Rayleigh scattering intensity across a convex flame cell as a function of position.

Figure 12: (b) Graph of normalised OH concentration and Rayleigh scattering intensity across a concave flame trough as a function of position.

narrow region where the curve drops from the large value associated with the low temperature unburned mixture, to the low value associated with the high temperature gas. The preheat zone thickness associated with a typical flame cell is estimated from Figure 12 (a) to be approximately 1.3 mm. The corresponding preheat zone thickness associated with one of the flame troughs is estimated from Figure 12 (b) to be approximately 3.0 mm.

Figure 13: (a) OH concentration, (b) Rayleigh scattering from a 2 bar, $\phi = 1.9$ iso-octane-air explosion flame (diameter ~ 100 mm).

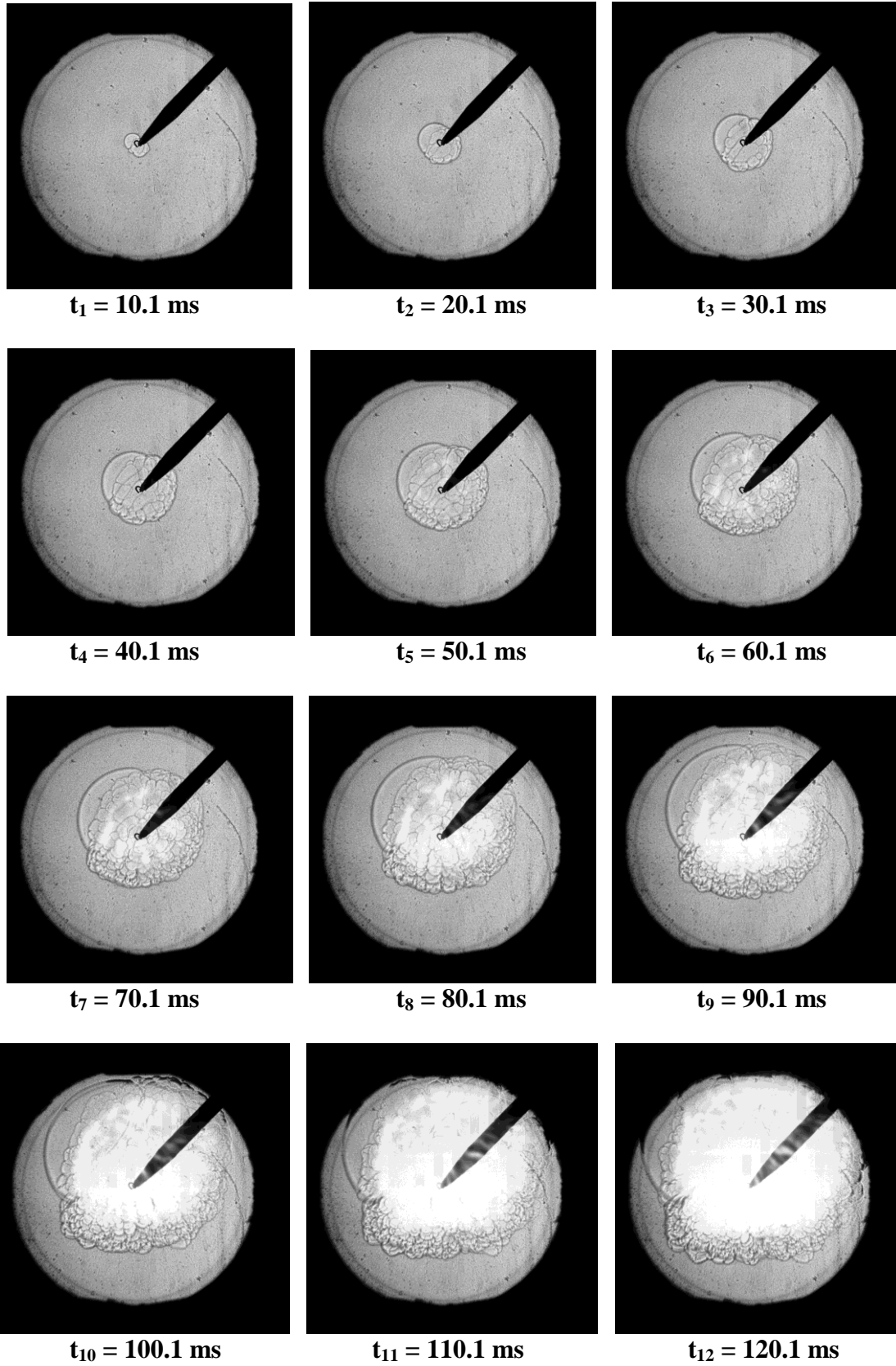**3.4 Structure of the 2 bar, ϕ = 1.9 Iso-octane-Air Laminar Explosion Flame**

Figures 13 (a) and 13 (b) show a processed OH concentration field and a processed Rayleigh scattering image obtained from a ϕ = 1.9 (C/O = 0.608) iso-octane-air flame with a radius of approximately 48 mm. High intensity elastic scattering from soot can be observed at the base of the deepest flame crack observable in Figure 13 (b). The two processed images constituting Figure 13 show many of the same features as the processed images displayed in Figure 11.

3.5 Dynamics and Structure of the 2 bar, ϕ = 2.0 Iso-octane-Air Laminar Explosion Flame
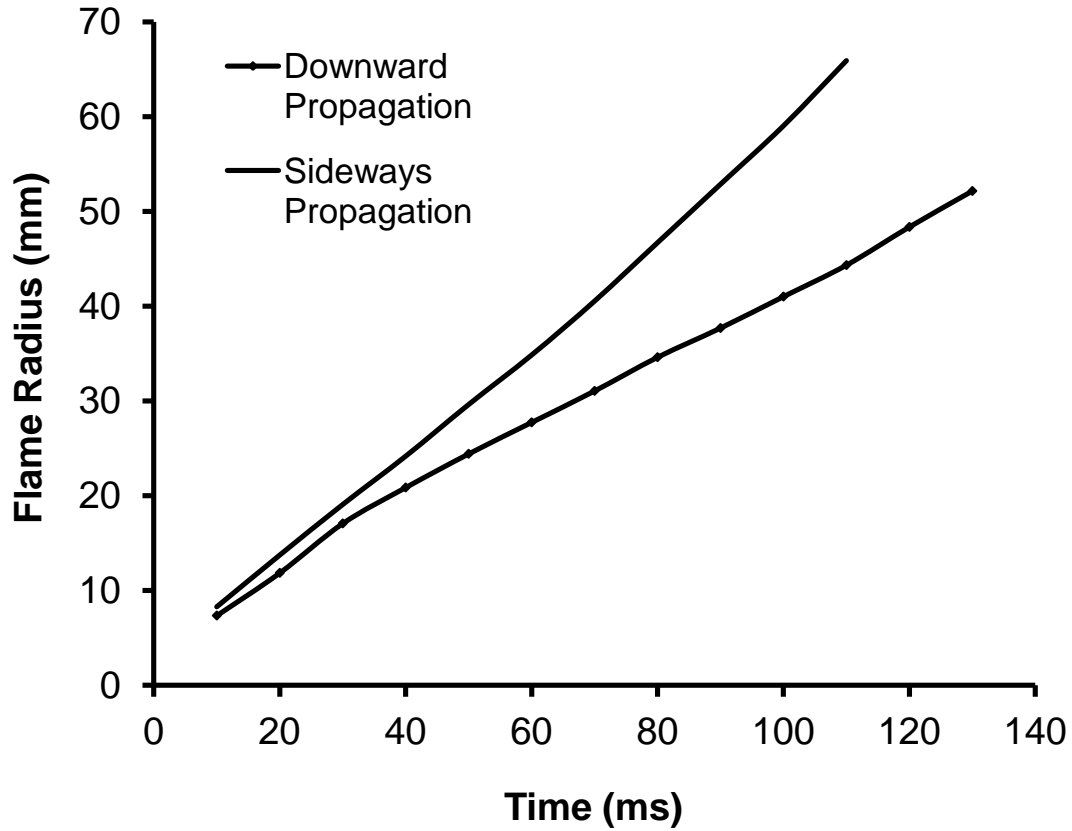
Figure 14 shows twelve shadowgraph images of a 2 bar, ϕ = 2.0 (C/O = 0.64) spherically expanding iso-octane-air explosion flame. The first image presented was obtained at 10.0 ms after the ignition pulse. The following images are shown at 10.0 ms intervals. Flame cellularity is observed to begin at $t \sim$ 50 ms (frame 5 of Figure 14), when the flame diameter is approximately 30 mm. The flame is buoyant, which causes the upper surface to expand with a larger radial expansion velocity than the lower surface (i.e. the centre of mass of burned gas rises with time).

Shadowgraph image frames 6 – 12 of Figure 14 are subject to white light contamination. This optical contamination is the result of broad-band grey body radiation emitted from soot formed behind the flame. The position and intensity of the white light contamination of the shadowgraph images reflect where the soot is formed behind the flame front, and the integrated amount of soot formed.

Figure 15 shows a graph of expanding flame radius with time, obtained from the ϕ = 2.0 flame shown in Figure 14. The smooth curve corresponds to the plot of mean radial expansion sideways versus time, while the data curve with points corresponds to the plot of radial expansion downwards versus time. The difference between the two plots demonstrates the effect of buoyancy on the expanding flame surface. The rate of radial expansion sideways and downwards is nearly constant over the radius range 10 mm $< r$ $<$ 75 mm. The downward radial expansion observable in Figure 14 corresponds to a flame expansion velocity of 0.38 ± 0.02 m/s.
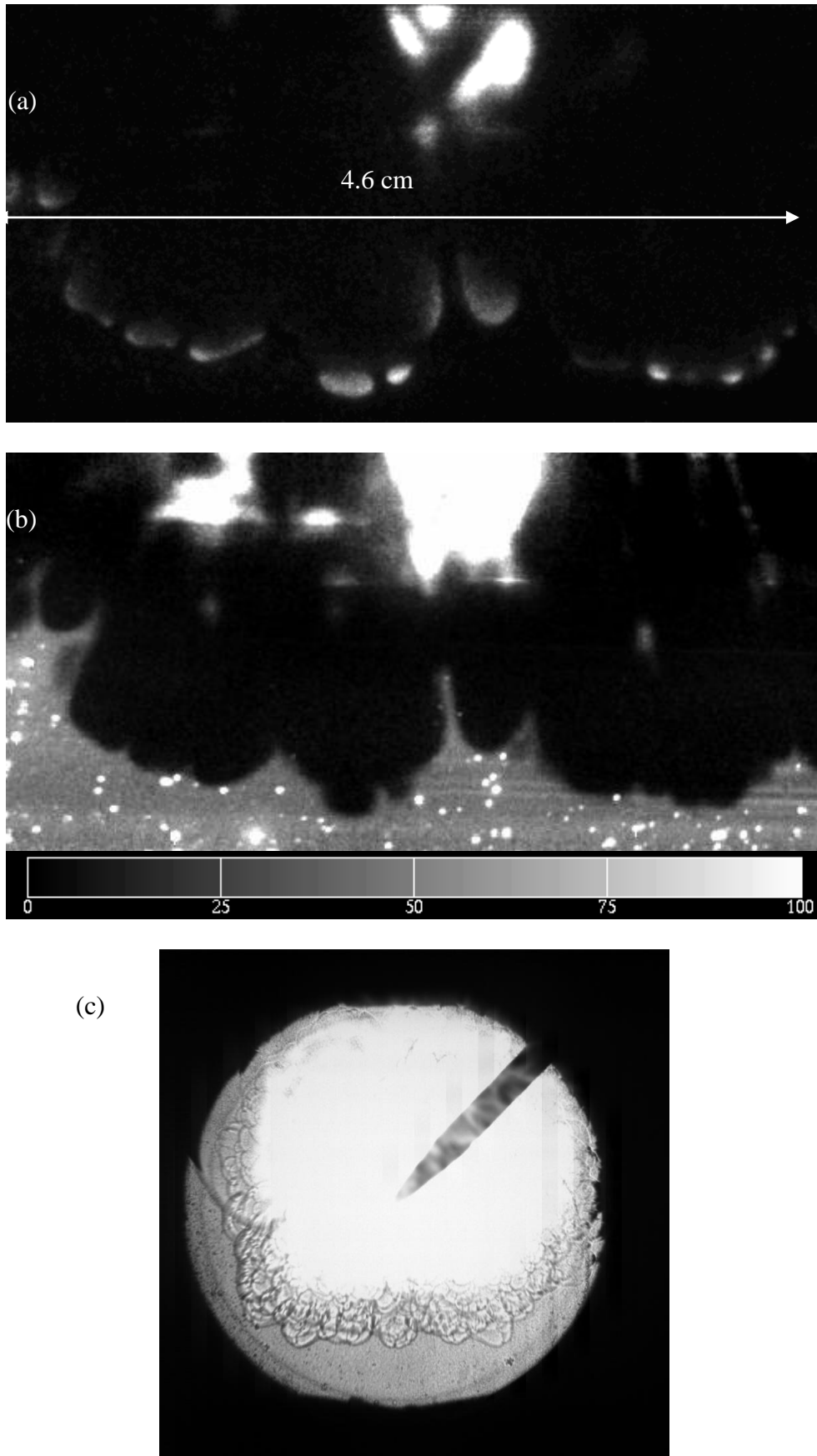
Figure 14: Shadowgraph images of a 2 bar, ϕ = 2.0 iso-octane-air explosion flame (window diameter = 15.0 cm).

Figure 15: Graph of Radial Flame Expansion (2 bar, $\phi = 2.0$ iso-octane-air explosion flame) versus Time.

Figures 16 (a) and (b) show the processed Rayleigh scattering image, together with the OH concentration field for a $\phi = 2.0$ explosion flame with a radius of approximately 54 mm. Elastic scattering from soot can be observed in Figure 16 (b), revealed as the regions behind the flame front associated with large scattering intensity. The elastic scattering from the soot on the Rayleigh image (Figure 16 (b)) has saturated the ICCD detector. Optical contamination of the processed OH fluorescence image can be observed in Figure 16 (a), a result of laser induced incandescence and filtered elastic scattering emitted from laser-heated soot formed behind the cellular flame front. The differences in the imaged soot structures are a consequence of the optical filtering of the 283 nm elastic scattering, the high emission threshold required for imaging soot incandescence at 308 nm, and elastic scattering d^6 dependence for small, newly formed soot particles.

Figure 16: (a) OH concentration, (b) Rayleigh scattering, (c) Shadowgraph image of a 2 bar, φ = 2.0 iso-octane-air explosion flame (flame diameter ~ 160 mm).

4. DISCUSSION OF RESULTS

4.1 The 2 bar, $\phi = 1.4$ Laminar Explosion Flame

Considering Figures 2 and 3 together reveal that when the $\phi = 1.4$ flame undergoes the transition to cellularity (diameter ~ 95 mm), the flame velocity is observed to increase from 2.35 m/s at 40 mm radius to 3.02 m/s at 70 mm radius. This observation is consistent with other findings [21].

A comparison of both Rayleigh scattering profiles and OH profiles in Figure 5 reveals that both the preheat zone and the reaction zone are much broader across a typical concave flame trough than across a typical convex flame cell crest. In addition the peak OH concentration in a flame trough is approximately 0.4x the peak OH concentration in a flame cell crest at this equivalence ratio. These observations are consistent with a lower rate of fuel oxidation and a lower flame speed occurring in a concave flame trough relative to that occurring in a convex flame cell crest.

A consideration of the Rayleigh scattering profiles in Figure 5 reveal that the high temperature CO and H oxidation to CO_2 and water continues up to approximately 15 mm behind the flame front. The burned mixture reaches full equilibrium when the distance behind and normal to the flame front is greater than this.

4.2 Cellularity and Oxidation in Rich Iso-octane-Air Explosion Flames

The peak OH to equilibrium OH ratio data shown in Figure 7 demonstrates the response of rich iso-octane-air flames to the thermal-diffusive instability in terms of flame structure, and local rate of oxidation and heat release. According to the linear model describing this type of instability [2, 4, 7], oxygen molecular diffusion into the convex flame surface dominates the heat diffusion from the convex flame surface. This results in a larger local OH concentration, an increased local rate of oxidation and increased local rate of heat release to occur in the convex parts of the flame surface (identifying flame cells), and lower local OH concentration, decreased local rate of oxidation and decreased local rate of heat release in the concave parts of the flame surface (identifying flame troughs or cusps). The approximately linear growth in the peak OH to equilibrium OH ratio and the reduction in peak OH to equilibrium OH in the flame

cusps with increasing equivalence ratio demonstrates the response of rich cellular flames to the increased dominance of oxygen diffusion relative to heat diffusion in the convex flame surface, and the depletion of oxygen in the fuel-air mixture entering the concave flame cusps.

Figures 5 and 12 indicate that the preheat zone thickness across the convex flame surfaces (flame cells) is significantly smaller that the preheat zone thickness across the flame cusps, and the local OH concentration in the reaction zone behind the convex flame surfaces is much larger than the local OH concentration found behind the adjacent cusps. This suggests that the local flame velocity of the convex flame surfaces (flame cells) is much larger than the local flame speed in the flame cusps. The cusps are observed to propagate together with the convex flame surfaces (flame cells). This suggests that the cusps propagate with the flame front as a result of molecular and heat diffusion from the reaction zones in the flame cells to the adjacent cusps. For large equivalence ratios, it might be suggested that the flame is locally quenched in the cusps as a result of local oxygen depletion and very large negative curvature.

It was identified from Figure 4 and Figure 11 that the mean thermal-diffusive cell size was observed to decrease for increasing equivalence ratio. This effect has been observed in other experiments, but is reported here for the first time. It is expected to occur as a response to increasing equivalence ratio, and decreasing oxygen mole fraction, a result of the increasing importance of the diffusion of oxygen away from the streamlines entering the flame cusps, towards the convex flame cells (regions of large OH concentration, rate of fuel oxidation and heat release). Paper 2 in the series will include a detailed length scale analysis and explanation of this effect.

4.3 Heat and Species Diffusion, and Soot Formation in the $\phi = 1.8$ Laminar Explosion Flame

The mean flame radial expansion velocity downward for the $\phi = 1.8$ flame was measured to be 0.79 ± 0.03 m/s. The flame crack observable in Figure 11 (a) and 11 (b) was approximately 10 mm deep, providing a flow residence time for oxygen depletion of approximately 12 ms. The soot formed behind the crack was initiated approximately

7 mm behind the cusp. The residence time for iso-octane pyrolysis and slow oxidation leading to soot formation was therefore estimated at approximately 8 ms.

A working hypothesis for the mechanism of incipient soot formation in rich iso-octane-air explosion flames at the critical equivalence ratio for soot formation is suggested, and can be summarised as follows. Streamlines of rich mixture nearing deep flame cusps experience further enrichment through a depletion of molecular oxygen diffusing towards the adjacent flame front. The deep cusps formed as a result of the interaction between the hydrodynamic instability and the thermal-diffusive instability are up to an order of magnitude deeper than the cusps associated with the thermal-diffusive instability. The fluid elements of fuel-air mixture following a streamline into the deep cusps are consequently depleted of oxygen up to an order of magnitude larger than the depletion occurring adjacent to normal cusps, a result of the increased residence time of the fluid element moving towards the deep cusp. The highly enriched iso-octane-air mixture enters the deep flame cusp, and is heated to pyrolysis temperatures through thermal diffusion. Iso-octane pyrolysis and slow oxidation results in the formation of olefins, acetylenes and aromatic hydrocarbons. The reaction of aromatics and acetylenes results in the formation of soot precursors, followed by small soot particles [18].

It is important to emphasize the role that local molecular diffusion plays in species and heat diffusion, and soot formation in the burned gas behind the cellular flame front. The uniformity of the Rayleigh scattering data behind the flame front suggests that both radial and tranverse heat diffusion occurs rapidly. Low mass species such as hydrogen atoms and molecules are likely to dominate the diffusion of heat behind the flame front. This should be contrasted with the slow local rate of diffusion of large mass hydrocarbon radicals, which results in local stratification of heavy hydrocarbon radicals behind flame cusps. Sufficient concentrations of these radicals, and low local concentrations of OH and O results in recombination reactions that form olefins, and acetylenes, followed by aromatics and soot particles.

4.4 Soot Formation in the $\phi = 2.0$ Laminar Explosion Flame

Figure 16 indicates that the soot formation regions are observed to develop behind more of the flame cusps. This suggests that fuel enrichment of the local mixture entering the thermal diffusive cell cusps has increased beyond the critical limit, enabling soot formation. The flame cells have a distribution of sizes between 1 mm and 3 mm, slightly smaller than those obtained in the $\phi = 1.8$ flame. The mean flame radius downward expansion velocity for the $\phi = 2.0$ flame was determined to be 0.38 ± 0.02 m/s at r ~ 50 mm. The soot formed behind the crack was initiated approximately 3 mm – 4 mm behind the cusp. This measurement is consistent with the distance separating the downward propagating flame front and the soot emission contamination observable in shadowgraph image Frame 12 of Figure 14. The residence time for iso-octane pyrolysis and slow oxidation leading to soot formation was therefore estimated at approximately 7.5 ms – 10 ms, consistent with the time-scale estimated earlier.

5. SUMMARY OF FINDINGS

1. The laminar explosion flames were observed to become unstable above a critical radius, developing a cellular structure over the entire surface. The radial flame expansion velocity was observed to increase at the critical radius for instability, as the flame became cellular.

2. Normalised equilibrium OH concentration measurements have been compared with normalised calculated equilibrium OH concentrations over the equivalence ratio range $1.4 \leq \phi \leq 2.0$, achieving agreement within experimental error. The equilibrium OH concentrations decrease exponentially as a function of equivalence ratio in the range $\phi = 1.4$ to $\phi = 2.0$.

3. The ratio of super-equilibrium OH concentration in the flame front to equilibrium OH concentration behind the flame front was discovered to increase linearly with equivalence ratio in the range $\phi = 1.4$ to $\phi = 2.0$, revealing the effect of differential heat and oxygen diffusion on the convex flame surface (flame cells) as a function of equivalence ratio.

4. Burned gas temperatures were estimated from the Rayleigh scattering data over the equivalence ratio range $1.4 \leq \phi \leq 1.9$, and compared with calculated isobaric adiabatic flame temperatures, achieving agreement within experimental error.

5. The preheat zone thicknesses across the convex flame surfaces were discovered to be significantly smaller (approximately 1.0 mm − 1.3 mm) than the preheat zone thicknesses across the concave flame cusps (approximately 2.5 mm − 3 mm). The Rayleigh scattering profile in the burned gas appeared uniform, suggesting a high degree of temperature homogeneity.

6. Mean flame cell size was observed to decrease with increasing equivalence ratio in the equivalence ratio range $1.4 \leq \phi \leq 2.0$.

7. The critical equivalence ratio for soot formation was observed to be $\phi = 1.8$ (C/O = 0.576). Soot was observed to form behind deep cracks in the flame surface. The distance between the base of the deep crack and soot behind the crack was found to be consistent with the distance between the flame surface and the white light contamination on the $\phi = 1.8$ and $\phi = 1.9$ shadowgraph images. A soot formation induction time of approximately 8 ms was estimated from the flame speed and the distance soot was observed behind the flame cusp.

8. At $\phi = 2.0$ (C/O = 0.64), the soot was observed to form behind more of the cusps in the flame surface. The distance required for soot formation behind the $\phi = 2.0$ flame front was measured to be 3 mm − 4 mm, consistent with the observations obtained from the Shadowgraph images. The timescale for iso-octane pyrolysis reactions leading to soot formation have been estimated to be 7 ms − 10 ms.

6. CONCLUSION

The experimental work presented in this paper has provided new insight into the dynamics and structure of high pressure, rich, iso-octane-air explosion flames. The data presented here will be useful to theorists, modellers, and experimental research engineers working on flame structure and soot formation in engines and combustors.

Equilibrium OH concentrations in the flames have been derived from OH laser induced fluorescence, and compared with theoretical equilibrium OH concentration as a function of equivalence ratio, achieving agreement within experimental error. In addition, burned gas temperatures have been obtained from Rayleigh scattering, and compared with theoretical isobaric adiabatic flame temperatures as a function of equivalence ratio, achieving agreement within experimental error. These results provided confidence in the validity of the other related data presented here.

The rich, high pressure, iso-octane-air explosion flames subjected to investigation were observed to develop a cellular surface above a critical radius, corresponding to a critical Peclet number. The mean cell size was observed to decrease with increasing equivalence ratio. This will be analysed in some depth in Paper 2 of this series, which undertakes a detailed analysis of relevant length scales associated with high pressure cellular flames.

The super-equilibrium OH to equilibrium OH concentration ratio was observed to increase linearly with increasing equivalence ratio, revealing the response of these flames to changing heat and molecular diffusion. The preheat zone thickness was observed to be much smaller across flames cells than across flame cusps. This revealed that the local flame speed at the cell surface was much larger than at the cusps. It was suggested that the flame cusps propagate with the convex flame surface as a result of molecular and heat diffusion from the reaction zones in the convex flame cells to the adjacent cusps. Indeed, at large equivalence ratios, it appeared that the cellular flames were effectively quenched in the cusps, a result of the very large negative curvature. Fuel entering the cusps was oxidised as a result of OH and heat diffusion from the reaction zones in the convex flame cells towards the adjacent cusps.

Soot was observed to form in explosion flames for $\phi \geq 1.8$ (C/O ≥ 0.546), forming a honeycomb-like structure behind the flame surface. Incipient soot was observed to form behind deep cusps in the flame surface, believed to develop as a result of short wavelength cells formed by the thermal-diffusive instability coupling to long wavelength cells formed by the hydrodynamic instability.

A working hypothesis for incipient soot formation for $\phi = 1.8$ explosion flames based on the experimental results has been proposed: the fuel-air mixture following streamlines into these deep cusps experience significant oxygen depletion through oxygen molecular diffusion into the adjacent flame surface, thereby enriching the local mixture entering the cusp. Slow oxidation and heating of the iso-octane leads to pyrolysis, resulting in alkane radical recombination, forming olefins and acetylenes. These in turn react to form simple aromatics, followed by polycyclic aromatic hydrocarbons (PAHs), followed by small soot particles. In contrast to the apparent thermal homogeneity in the burned gas, the heavy alkane radicals formed behind the flame cusps remain locally stratified, to eventually contribute to soot formation. The induction time for soot formation to occur was measured to be approximately 8 ms.

Finally, soot formed in the $\phi = 2.0$ flame was observed to occur behind more of the flame cusps, suggesting that local enrichment of the fuel was large enough and local oxidation of the fuel and radicals was low enough for local fuel pyrolysis to result in soot formation. Soot formation induction times were again estimated to be in the range of 7.5 ms – 10 ms.

The experimental results presented in this paper should form a basis for future theoretical work and/or model development. The working hypotheses require testing through further experimental work and modelling.

ACKNOWLEDGEMENTS

REFERENCES

1. D. Bradley, C.G.W. Sheppard, R. Woolley, D.A. Greenhalgh, R.D. Lockett, Combust. Flame 122 (2000) 195 – 210.

2. M. Matalon, Ann. Rev. Fluid Mech. 39 (2007) 163 – 191.

3. G. Jomaas, C. K. Law, J. K. Bechtold, J. Fluid Mech. (2007) in press.

4. M. Hertzberg, Prog. Ener. Combust. Sci. 15 (1989) 203 – 239.

5. G.H. Markstein, Proc. Combust. Inst. 4 (1953) 44.

6. A. Palm-Leis, R.A. Strehlow, Combust. Flame 13 (1969) 111.

7. C.K. Law, G. Jomaas, J.K. Bechtold, Proc. Combust. Inst. 30 (2005) 159 – 167.

8. R. Lockett, J. Phys.: Conf. Series 45 (2006) 154 – 160.

9. D. Bradley, M. Lawes, Kexin Liu, S. Verhelst, R. Woolley, Combust. Flame 149 (2007) 162 – 172.

10. R.D. Lockett, R. Morishima, R. Woolley, to be submitted to Combustion and Flame (2007).

11. G. Patnaik, K. Kailasanath, E.S. Oran, K.J. Laskey, Proc. Combust. Inst. 22 (1992) 1517.

12. S. Kadowski, T. Hasegawa, Prog. Ener. Combust. Sci. 31 (2005) 193 – 241.

13. J. Yuan, Y. Ju, C.K. Law, Proc. Combust. Inst. 31 (2007) 1267 – 1274.

14. I. Kennedy, Prog. Ener. Combust. Sci. 23 (1997) 95 – 132.

15. H. Zhao, N. Ladommatos, Prog. En. Combust. Sc. 24 (1998) 221 – 255.

16. H. Richter, J.B. Howard, Prog. Ener. Combust. Sc. 26 (2000) 565 – 608.

17. A. Leipertz, F. Ossler, M. Alden, Applied Combustion Diagnostics, Taylor & Francis, ed. K. Kohse-Hoinghaus, J. Jeffries (2002) 359 – 383.

18. C.S. McEnally, L.D. Pfefferle, B. Atakan, K. Kohse-Hoinghaus, Prog. En. Combust. Sc. 32 (2006) 247 – 294.

19. D.R. Tree, K.I. Svensson, Prog. Ener. Combust. Sc. 33 (2007) 272 – 309.

20. N. Tait, Combust. Flame 117 (1998) 435 – 437.

21. T. Duverger, Unpublished Work, PSA Peugot-Citroen (1997).

22. L. Gillespie, M. Lawes, C. Sheppard, R. Woolley, SAE Paper 2000-01-0192 (2000).
23. R.D. Lockett, unpublished work (2007).

24. C. Olikara, G. Borman, SAE Paper 750468 (1975).

25. B. Rogg, RUN-1DL, Cambridge (1994).

26. A. S. Al-Shahrany, D. Bradley, M. Lawes and R. Woolley, Proc. Combust. Inst. 31, (2005) 225 – 232.

27. D. Bradley, R.A. Hicks, M. Lawes, C.G.W. Sheppard, R. Woolley, Combust. Flame 115 (1998) 126 – 144.

28. A. Koch, H. Voges, P. Andresen, H. Schluter, D. Wolff, W. Hentschel, W. Opperman, E. Rothe, Appl. Phys. B 56 (1993) 177 – 184.

29. A.Taylor (Ed), Instrumentation for Flows with Combustion, Academic Press Ltd (1993) 468.